Article

Not peer-reviewed version

SISA: The First Extreme-Ultraviolet Solar Integral Field Spectrograph Using Slicers

Ariadna Calcines Rosario * , Hamish Andrew Sinclair Reid , Sarah Matthews , Frédéric Auchère , Alain Jody Corso , Giulio Del Zanna , Jaroslav Dudik , Samuel Gissot , Laura Hayes , Graham Stewart Kerr , Christian Kintziger , Sophie Musset , Vanessa Polito , Daniel F. Ryan , David Orozco Suárez

Posted Date: 29 November 2023

doi: 10.20944/preprints202311.1854.v1

Keywords: EUV Spectroscopy; solar IFS; EUV slicers; image slicers; solar space mission; particle acceleration

Article

SISA: The First Extreme-Ultraviolet Solar Integral Field Spectrograph Using Slicers

Ariadna Calcines Rosario [1,*], Hamish A. S. Reid [2], Sarah Matthews [2], Frederic Auchère [3], Alain Jody Corso [4], Giulio Del Zanna [5], Jaroslav Dudík [6], Samuel Gissot [7], Laura A. Hayes [8], Graham S. Kerr [9,10], Christian Kintziger [11], Sophie Musset [8], Vanessa Polito [12,13], Daniel F. Ryan [14] and David Orozco Suárez [15,16]

1 Durham University, Centre for Advanced Instrumentation, Department of Physics, Durham, UK.
2 University College London, Mullard Space Science Laboratory, Holmbury Hill Rd, Dorking RH5 6NT, United Kingdom
3 Université Paris-Saclay, CNRS, Institut d'Astrophysique Spatiale, 91405, Orsay, France
4 National Research Council of Italy, Institute for Photonics and Nanotechnologies, via Trasea 7, 35131, Padova, Italy
5 Department of Applied Mathematics and Theoretical Physics, University of Cambridge, Wilberforce Road, Cambridge CB3 0WA, United Kingdom
6 Astronomical Institute of the Czech Academy of Sciences, Fričova 298, 251 65 Ondřejov, Czech republic
7 Royal Observatory of Belgium, Ringlaan -3- Av. Circulaire, 1180 Brussels, Belgium
8 European Space Agency, ESTEC, Keplerlaan 1 - 2201 AZ, Noordwijk, The Netherlands
9 NASA Goddard Space Flight Center, Heliophysics Science Division, Code 671, Greenbelt, MD 20771, USA
10 Department of Physics, Catholic University of America, Washington DC 20064, USA
11 Centre Spatial de Liège, University of Liège (ULiège) – STAR Institute, Liège, Belgium
12 Lockheed Martin Solar and Astrophysics Laboratory, Building 252, 3251 Hanover Street, Palo Alto, CA 94304, USA
13 Department of Physics, Oregon State University, Corvallis, OR 97333, USA
14 University of Sciences and Arts Northwest Switzerland (FHNW), Bahnhofstrasse 6, Windisch 5210, Switzerland
15 Spanish Space Solar Physics Consortium (S^3PC)
16 Instituto de Astrofísica de Andalucía (IAA-CSIC), Granada, Spain
* Correspondence: ariadna.calcines@durham.ac.uk

Abstract: Particle acceleration, and the thermalisation of energetic particles, are fundamental processes across the universe. Whilst the Sun is an excellent object to study this phenomenon, since it is the most energetic particle accelerator in the Solar System, this phenomenon arises in many other astrophysical objects, such as active galactic nuclei, black holes, neutron stars, gamma ray bursts, solar and stellar coronae, accretion disks and planetary magnetospheres. Observations in the Extreme Ultraviolet (EUV) are essential for these studies but can only be made from space. Current spectrographs operating in the EUV use an entrance slit and cover the required field of view using a scanning mechanism. This results in a relatively slow image cadence on the order of minutes to capture inherently rapid and transient processes, and/or in the spectrograph slit 'missing the action'. The application of image slicers for EUV integral field spectrographs is therefore revolutionary. The development of this technology will enable observations of EUV spectra from an entire 2D field of view in seconds, over two orders of magnitude faster than what is currently possible. The Spectral Imaging of the Solar Atmosphere (SISA) instrument is the first integral field spectrograph proposed for observations at $\sim$ 180 Å combining the image slicer technology and curved diffraction gratings in a highly efficient and compact layout, while providing important spectroscopic diagnostics for characterization of solar coronal and flare plasmas. SISA's characteristics, main challenges and the on-going activities to enable the image slicer technology for EUV applications are presented in this paper.

Keywords: EUV spectroscopy; solar IFS; EUV slicers; image slicers; solar space mission; particle acceleration

 doi:10.20944/preprints202311.1854.v1

1. The Need for Solar Integral Field Spectrometers in the Extreme Ultraviolet

Particle acceleration is a fundamental process arising in many astrophysical objects including active galactic nuclei, black holes, neutron stars, γ ray bursts, accretion disks, solar and stellar coronae, and planetary magnetospheres.

In our solar system, the Sun is the most energetic particle accelerator. Its proximity makes it a unique laboratory with which to explore the physics of energetic particles, which has wider importance in understanding astrophysical particle acceleration more generally. However, despite its importance and past observations, the physics underlying solar particle acceleration remains poorly understood. For the study of solar particle acceleration and the evolution of solar eruptive events (solar flares and coronal mass ejections; CMEs), it is useful to observe in the Extreme Ultraviolet (EUV) regime, since this wavelength range contains a number of emission lines that allow the corona and transition region to be probed and whose profiles allow the presence of non-Maxwellian particle distributions to be diagnosed. Additionally, the plasma response following the thermalisation of these energetic particles can be dramatic, with resultant heating, ionisation, mass flows, and turbulence, all of which can be diagnosed with EUV spectroscopic observations. The plasma in the solar corona is typically fully ionised because of the megaKelvin plasma temperatures. Such hot plasma contains ions that emit brightly in EUV wavelengths ($\lambda \sim 100 - 1200$ Å).

Measurements in the EUV can be used to characterise the temperature, density, elemental composition and the turbulent state of the plasma in the upper solar atmosphere, for both the quiet and active Sun. Plasma density can be diagnosed through the observation of density sensitive line ratios in all coronal features, from the quiet Sun and coronal holes to active regions, flares, jets and coronal mass ejections. Measurements of densities in the corona are fundamental for understanding how the corona is heated. Moreover, they are key for understanding how the solar corona transitions into the solar wind. Measuring electron densities during transient processes like solar flares also allows us to understand the timescales of ionisation processes that occur during the conversion of magnetic to kinetic energy (which in the standard solar flare model occurs following magnetic reconnection).

The traditional method for performing solar imaging spectroscopy in the EUV [e.g. 1,2] has been to use a slit spectrometer and a scanning mechanism to cover a larger field of view. Whilst 'sit-and-stare' observations can be produced within seconds for a strongly emitting EUV line from one location, the traditional slit scanning spectrometer takes minutes to create a spectrum across a 2D spatial region of the Sun depending on the desired field of view. Using integral field spectroscopy (IFS), all spectra of a 2D field of view will be obtained simultaneously, reducing the integration time by over two orders of magnitude and without the requirement for any rastering mechanism. We also note that a novel solar ultraviolet IFS concept will be used for the first time during the Solar eruptioN Integral Field Spectrograph (SNIFS) NASA sounding rocket launch in Spring 2024 [3,4].

2. SISA Science in the SPARK Framework

SISA is envisioned as one component of a suite of complementary instruments that together form the The Solar Particle Acceleration Radiation and Kinetics (SPARK) mission concept, along with the Large Imaging Spectrometer for Solar Accelerated Nuclei (LISSAN) and the Focusing Optics X-ray Solar Imager (FOXSI) instruments both of which target high-energy x-ray and γ-ray emission. SPARK is designed to address the open questions regarding particle acceleration on the Sun.

SPARK will attack the problem of particle acceleration through a powerful combination of γ-ray, X-ray and EUV imaging and spectroscopy at high spectral, spatial, and temporal resolutions. In addition to helping in addressing the physics of particle acceleration, SISA shall provide critical measurements of plasma conditions (magnetic fields, temperatures, densities, and elemental composition) in the various coronal and flare structures, both pre- and post-reconnection. As these measurements are integral to understanding how the plasma responds to particle acceleration, and critical for understanding of how and when flares occur, the SISA EUV integral field spectrometer

 doi:10.20944/preprints202311.1854.v1

is an crucial addition to the SPARK mission. The significant advantage of SISA with respect to previous EUV spectrographs is that it will enable these crucial measurements in an integral field regime, i.e., spectroscopic measurements simultaneously over a wide field of view. Below, we briefly discuss how this instrument contributes to the key science goals to be addressed by the SPARK mission:

- **How does impulsive energy release accelerate particles in the solar atmosphere?**

  SISA shall provide several measurements of accelerated particles in EUV, both electrons through line ratios (see Section 3.2) and ions through line profiles (see Section 3.3). The integral field spectroscopy of SISA will offer insights as to where and when the particles are accelerated, while the fast cadence will reveal how long they persist at a given location. Measuring the spatial distribution of the accelerated particles, and their relationship to magnetic field (see Section 3.1) and field-aligned emission structures, will also offer insights as to the conditions required for particle acceleration, both in solar flares and active-region corona. The fast-cadence SISA observations with multiple hot lines (Table 1) shall also clarify the relationship of particle acceleration to plasma heating. Finally, since the emission line profiles reflect the line-of-sight distribution of ion velocities, from zero to very high velocities, they provide key information about both the high-energy particles simultaneously with the low-energy end of the distribution, not accessible with either LISSAN or FOXSI instruments.

- **How is impulsively released energy transported and dissipated in the solar atmosphere?**

  Once heated, the hot flare plasma evolves rapidly on short timescales depending on the conditions. The hot flare lines observed by SISA cover some of the largest available temperatures via EUV line spectroscopy (Table 1) and are thus favorable for characterizing the hot flare plasma and its evolution. Typically, the hot plasma is observed first above the chromospheric footpoints in the form of localized bright kernels [e.g., 5,6], from which the flare loops are filled. Indications however exist that these kernels located within bright flare ribbons can already be pre-heated by electron beams [7,8]. These kernels have been long observed to move along ribbons [e.g., 9–11], which have been identified as a consequence of 3D slipping reconnection [e.g., 12–18], where the field lines do not reconnect in an X-point, but slip (slide) past each other as they mutually exchange their connectivities [see, e.g., 19–21]. The existence of this process implies that the location of the energy deposition into the lower solar atmosphere changes with time as the slipping reconnection proceeds. In the past, it has been extremely difficult to identify the spectroscopic signatures of this process due to the slit not being able (or designed) to track a particular moving (slipping) kernel. Using sit-and-stare observations Li and Zhang [15] showed that the slipping reconnection is likely be related to periodic changes of Si IV spectral line intensities accompanied by enhanced redshifts, as well as increased nonthermal widths, as individual kernels moved through the location of the slit. Recently, Lörinčík *et al.* [18] detected extremely short-lived blueshifts (upflows), lasting only seconds, and reaching about 50 km s^{-1} in chromospheric and transition-region lines, at the leading edges of the slipping kernels. The authors argued that such detection can be a matter of luck with slit spectrographs, as the slit has to be in the right place at the right time. The IFS provided by SISA shall be enormously helpful in this regard, as it can image the entire flare region and allow us to identify how the flaring atmosphere undergoing slipping reconnection responds at short temporal cadences, as well as enable tracking the spectral evolution of individual moving kernels as they slip along flare ribbons. In addition, the SISA thermal coverage would help in establishing whether the blueshifts at the leading edges of ribbons or individual kernels are related to evaporation of hot flare plasma.

  The fastest upflow velocities of the evaporating hot flaring plasma filling coronal loops are detected in the hottest flare lines [5], while the 'cooler' ($T <\sim 1$ MK) lines show downflows at the same location, implying multi-directional flows that could occur due to rapid plasma evolution.

 doi:10.20944/preprints202311.1854.v1

The fast SISA cadence and the integral field spectroscopy, coupled with the available plasma diagnostics (Section 3) will provide key information on the thermal evolution of the heated plasma. For example, diagnostics of electron density coupled with the measured timescales of plasma cooling will allow for discerning whether the plasma is in ionization equilibrium, and at what times. Meanwhile, the emission line profiles will provide information on the presence and role of turbulence. Mass flows and the thermodynamic evolution of the atmosphere determined via spectroscopy can reveal much about the energy input to the lower atmosphere during flares, especially when combined with state-of-the-art modelling. For example, flare observations from the Interface Region Imaging Spectrograph [IRIS; 2,22] have been used in tandem with flare loop models to interrogate our understanding of flare processes [23,24]. A major model-data discrepancy is the duration of the flare gradual phase, with models under-predicting the cooling time by an order of magnitude. SISA observations that provide plasma diagnostics over the full field of view, with high cadence, will help illuminate the source of the continued heating or energy input. Measurements of nonthermal line widths from lines formed at different temperatures, will inform us about the roles of turbulence in suppressing thermal conduction [e.g. 25], and the potential role of Alfvén waves in flares [e.g. 26,27].

SISA measurements will provide key diagnostics of processes that occur within flares on short timescales. For example, a key open question in solar flare energy release is what drives "bursty" pulsations and oscillatory signatures observed in flare emission, known as quasi-periodic pulsations (QPPs) [see 28–30, for reviews]. QPPs and other oscillatory behaviour observed in flares have timescales ranging from sub-seconds to minutes, and are identified across the entire electromagnetic spectrum from radio, EUV [31], X-rays [32] and even γ-rays [33], essentially encompassing all aspects of the flaring process. The exact nature and underlying physical mechanism for the generation of these pulsations remains highly debated. It is suggested that they may be related to magnetohydrodynamic oscillations in/near the flare site, or possibly connected to the intermittent or time-dependent magnetic reconnection itself. Observational limitations to date of temporal cadences, spatial resolution, and saturation issues with EUV imagers have limited our ability to observational identify the locations of the emission modulations and constrain the suggested models - both of which are directly linked to energy release and transport in solar flares. Some work has aimed to identify the spatial locations of the modulations [e.g. 15,31,34–36], although they are limited temporal cadences, and the spatially diagnostics; for example only spatially observing along the slit position. In order to correctly identify the mechanism producing QPPs, characteristics of the temporal, spatial and spectral properties of pulsations and their relationships across energy ranges and temperatures are required. The SISA EUV measurements with high temporal cadence, and its ability to perfrom imaging spectroscopy of the flaring region (rather than just over the slit) will allow us to observe rapid changes in the flaring regions such as these pulsations, with information regarding *where* and at what *temperature* they originate in the flare structure.

Finally, though there is unambiguous evidence for the presence of nonthermal particles in flares, other mechanisms may also act to transport liberated magnetic energy. High frequency Alfvén waves have been proposed as a means of transporting energy the magnetic reconnection site to the lower atmosphere and heating it [e.g. 37–39]. Modelling has revealed that those waves do indeed heat the chromosphere, and drive explosive evaporation into the corona [40–42]. While it is likely that MHD waves are produced during flares, which are fundamentally a large scale change in the corona's magnetic field, the proportion of energy that manifests itself in the form of waves compared to energetic particles is not known. SISA's capability to measure the coronal magnetic field before, during and after a flare will provide crucial information regarding field perturbations, and together with density diagnostics the Alfvén speed, which will help to provide estimates of the Poynting flux carried by MHD waves. Furthermore, nonthermal broadening of ions will also help constrain the Poynting flux [see discussion in, e.g., 26].

 doi:10.20944/preprints202311.1854.v1

- **What are the physical low-corona origins of space weather events?**

  Both Coronal Mass Ejections (CMEs) and jets inject magnetic field and plasma into the heliosphere, where they disturb the solar wind flow. Although previous studies of CME source regions have provided details about the physical processes taking place once a CME has initiated, many questions remain regarding their initiation and similarities with smaller scale flux rope eruptions within solar jets. Observing the initiation of both CMEs and jets spectroscopically is quite difficult with current or planned instrumentation for several reasons, including the use of a single slit, long exposure times, or limited diagnostics and temperature coverage provided by the available spectral lines. SISA will capture these processes at cadences down to a few seconds from every pixel within its entire field of view. This will allow us to identify the locations, spectral properties, plasma conditions, and thus the mechanisms behind the processes of CME and jet initiations. In larger eruptive events, SISA will be able to capture the entirety of precursor phase of the associated flare. The spatial localization of the precursors with respect to the subsequent flare and eruption allows for identification of the CME initiation mechanism, whether by tether-cutting, ideal MHD instability, or breakout [see 43] for every flare observed. The high-temperature lines observed by SISA (Table 1) will provide information on the plasma properties during the onset of eruptive events, including the possibly constant, isothermal 10–15 MK onset temperatures detected by broad-band X-ray instrumentation [44]. These lines will also allow the quantification of plasma heating (via temperature and density measurements) as well as turbulence (via line broadening) in the precursor phase.
- **How is the corona above active regions heated?**

  It is currently thought that the solar corona is heated by individual impulsive "nanoflare" events that release small amounts of energy at either high or low frequencies [e.g., 45–49]. A key prediction of such impulsive energy release is the existence of small amounts of hot 5–10 MK plasma, which is difficult to detect spectroscopically with current instrumentation [50–55]. The spectral range of SISA contains several hot lines (Table 1) that will provide stringent constraints on the amount of plasma reaching 10 MK temperatures. The Fe XVII and Ni XVII lines (Table 1) shall provide additional constraints. SISA will also work in tandem with the HXR and SXR observations to constrain the high-T component of the impulsive energy release by nanoflares. Another key observable of impulsive energy release is that the plasma should at least temporarily be out of thermal equilibrium, showing either presence of accelerated particles, out-of-ionization equilibrium plasma [e.g., 56–59], or both. The coronal Fe XI lines formed in both quiet Sun and active regions offer such diagnostics for electrons [60,61] while the line profiles of multiple ionization stages shall provide information on ion velocity distribution [62–65]. Furthermore, temporal evolution of line intensities of multiple ionization stages obtained in high cadences in combination with electron density diagnostics (Section 3.7) shall provide information on both the presence of energy release events and constraints on the presence of non-equilibrium ionization for multiple coronal structures at the same time, a feat not possible with current or planned instrumentation. Finally, it will become possible for the first time to tie all these measurements to the measurements of the underlying magnetic field (Section 3.1), thus allowing for discerning whether there are different heating mechanisms for different magnetic structures within the active and quiescent solar corona.

Preprints (www.preprints.org) | NOT PEER-REVIEWED | Posted: 29 November 2023 doi:10.20944/preprints202311.1854.v1

Table 1. A selection of SISA diagnostic spectral lines. The approximate formation temperature (log T[K]) is shown, as well as the radiances for an AR core and an M2-class flare (in erg cm^{-2} s^{-1} sr $^{-1}$). Numbers in brackets are DN s^{-1} per 1″ SISA pixel.

Ion	λ (Å)	log T	AR core	M2 flare	Notes
Ni XV	178.89	6.5	15	1.2×10^2	
Fe XXI	178.90	7.1	-	4.8×10^2 (145)	** Flare Ne
Fe XI	179.76	6.1	130 (40)	9.0×10^2 (276)	** Ne
Fe XXIII	180.04	7.2	-	8.8×10^2 (270)	* Flare
Fe XI	180.40	6.1	1.4×10^3 (429)	3.1×10^3 (950)	** (bl Fe X)
Ca XV	181.90	6.5	-	4.2×10^2 (156)	*** Ne
Fe XI	182.17	6.1	120 (47)	1.1×10^3 (429)	*** Ne
Ca XV	182.86	6.5	-	6.4×10^2 (310)	*** Ne
Fe X	184.54	6.0	220 (175)	5.5×10^2 (439)	*** Coronal B
Fe XI	184.79	6.1	76 (64)	5.0×10^2 (424)	*** Ne
Fe XII	186.89	6.2	600 (395)	2790 (1836)	(bl) ** Ne
Fe XXI	187.93	7.1	-	3.8×10^3 (1172)	*** Flare (bl Ar XIV)
Ar XIV	187.96	6.5	21	3.4×10^2	** Ne, FIP
Fe XI	188.22	6.1	710 (160)	1.6×10^3 (362)	***
Ar XV	221.15	6.5	73 (13)	3.4×10^3 (584)	*** FIP
Fe XXIII	221.34	7.2	-	5.6×10^2 (100)	Flare
S XII	221.43	6.4	90 (16)	4.1×10^2 (75)	** FIP
Fe XV	233.87	6.5	260 (247)	3.0×10^3 (2850)	** Ne
Fe IX	241.74	5.9	120 (189)	120 (189)	*** Ne
Fe XXI	242.05	7.1	-	4.1×10^3 (6540)	*** Flare Ne
He II	243.03				
Ar XIV	243.75	6.4	43	5.3×10^2	FIP (bl)
Fe XV	243.79	6.5	880 (1502)	6.5×10^3 (11095)	(bl Ar XIV)
Fe IX	244.91	5.9	80 (141)	2.3×10^2 (406)	*** Ne
Fe XXI	246.95	7.1	-	6.5×10^2 (1205)	*** Flare
Fe XXII	247.19	7.1	-	8.0×10^3 (14887)	*** Flare
Ar XIII	248.68	6.2	7 (13)	1.1×10^2 (209)	** FIP
Ni XVII	249.19	6.6	840 (1598)	9.3×10^3 (17690)	*** Flare
Fe XII	249.39	6.2	65 (124)	2.4×10^2 (457)	
Fe XVI	251.06	6.5	650 (1234)	1.0×10^4 (18979)	
Fe XIII	251.95	6.2	460 (864)	1.7×10^3 (3194)	
Fe XIV	252.20	6.4	280 (524)	1.8×10^3 (3367)	
Fe XXII	253.17	7.1	-	3.9×10^3 (7177)	*** Flare
Fe XVII	254.88	6.6	-	3.5×10^3 (6140)	*** Flare
Fe XXIV	255.11	7.3	-	4.8×10^4 (83656)	*** Flare
He II	256.3				(bl)
S XIII	256.68	6.5	1.1×10^3 (1797)	8.6×10^3 (14055)	** FIP
Fe X	257.26	6.0	140 (222)	150 (238)	*** coronal B
Fe XIV	257.39	6.4	420 (663)	2.1×10^3 (3317)	
Fe XI	257.55	6.1	80 (125)	2.3×10^2 (360)	** Te,NMED
Si X	258.37	6.2	420 (628)	1.5×10^3 (2243)	Ne
S X	259.50	6.2	53 (74)	1.8×10^2 (251)	*** FIP
Si X	261.06	6.2	140 (175)	4.2×10^2 (525)	Ne
Fe XVI	262.98	6.5	1.1×10^3 (1148)	1.7×10^4 (17754)	
Fe XXIII	263.77	7.2	-	2.1×10^4 (20192)	*** Flare
S X	264.2	6.2	77 (71)	257 (237)	*** FIP

3. SISA EUV Measurements and Diagnostics

Based on these scientific cases, two spectral windows have been defined for SISA: $\lambda = [178 - 184]$ Å and $\lambda = 246 - 258$ Å. There are numerous EUV spectral lines originating from a range of

 doi:10.20944/preprints202311.1854.v1

species that together allow a wide temperature coverage from transition region through to coronal and flare plasma. Many density sensitive line pairs are included within these windows, including at $T > 10$ MK, as are a pair of Fe X transitions whose ratio is proportional to the coronal magnetic field strength. Via the inclusion of Fe XI the electron temperature and presence of non-Maxwellian electron distributions can be probed. There are also transitions of S and Ar to measure the FIP bias, relative to Fe lines, providing vital composition information.

Table 1 lists the spectral lines of interest, along with notes regarding the diagnostics they provide. There is some overlap with the EUV spectral lines observed by *Hinode*/EUV Imaging Spectrograph [EIS; 1], but with higher sensitivity, cadence, and simulataneous spatial coverage [for more details see, e.g. 66]. Whilst EIS requires an estimated 50 minutes to scan a 100″ region with its 2″ slit and 60 s exposures to obtain enough signal for coronal magnetic field measurements, SISA would obtain the same observations within a few seconds.

Once they thermalise, the energetic particles that carry flare energy from the corona to the transition region and chromosphere, heats the local plasma. The intense heating subsequently leads to ionisation and drives mass flows: so-called chromospheric evaporation and condensation. Spectral lines from species forming at different temperatures are very useful in diagnosing the conditions of the plasma before, during, and after energy deposition. They can reveal gradients in density, bulk velocity and temperature. We have typically been restricted to observations in single locations, whether that be at the flare footpoints, along the loops, or at looptops. However, to understand the full story of where flare energy is deposited and how the plasma responds, simultaneous observations, at high-cadence, of the full flaring structure would be transformative.

3.1. Magnetic Field Measurements

The solar coronal magnetic field can be measured via the recently identified Fe X 184.54 /257.26 Å line intensity ratio [see, e.g. 67–69]. While the former line is an allowed transition, the latter, Fe X 257.26 Å, is a blend of several intercombination transitions. In the presence of the external magnetic field, a new decay channel to the ground configuration $3s^2\,3p^5\,{}^2P_{2/2}$ occurs due to mixing of the upper metastable levels $3s^2\,3p^4\,3d\,{}^4D_{7/2}$ and $3s^2\,3p^4\,3d\,{}^4D_{5/2}$ [70]. This magnetically-induced transition (MIT) increases the intensity of the 257.26 Å line, and allows for measurements of coronal magnetic field. This has already been done using the solar EUV spectra measured by Hinode/EIS, revealing presence of magnetic fields of up to several hundred Gauss in a C2-class flare [70] as well as in the solar coronal loops [71].

However, making such measurements routine using slit spectroscopy (as in the case of Hinode/EIS) is difficult, as the slit only samples a small portion of the solar atmosphere. In addition, the Fe X line at 256.26 Å is relatively weak, requiring long exposure times with previous instruments such as EIS. Finally, the diagnostic ratio is also sensitive to a range of parameters, as the electron density and temperature, so additional diagnostic lines are needed. They are provided by SISA, as described below.

The SISA instrument shall allow for routine measurements of both Fe X lines in a wide field of view and at orders of magnitude faster cadence, providing revolutionary potential for magnetic field measurements both before, during, and after the reconnection process; that is, from the active region corona pre-reconnection to the post-reconnection flare loops. Such measurements will allow for the first time to provide a direct measurement of the magnetic energy released during the flare reconnection.

3.2. Electron temperature and nonthermal diagnostics

To measure the result of transport effects on accelerated electrons, the nonthermal electron spectrum must be characterised at multiple locations in the flare structure, namely near the acceleration region, along the flare loops, and near the chromospheric footpoints.

 doi:10.20944/preprints202311.1854.v1

SISA's wavelength range contains lines of multiple Fe ions (see Table 1) from Fe IX formed at upper transition region, Fe X, Fe XI, Fe XIV, and Fe XVI formed in the corona of quiet Sun and active regions, to multiple flare lines of Fe XXI, Fe XXII, and Fe XXIV. Such wide temperature coverage shall allow for characterization of the ionization temperature of the plasma, and in particular the coronal structures participating in the reconnection process, from the pre-reconnection corona to post-reconnection flare loops.

In addition, the EUV lines observed by SISA allow to assess if nonthermal electrons are present in certain cases. The ratios of Fe XI line intensities at 182.17 / 257.55 Å 182.17 / 257.77 Å are sensitive to high-energy electrons at temperatures above 1 MK [60,72]. The Fe XI lines at 257.55 Å and 257.77 Å are located in direct vicinity of the magnetically-sensitive Fe X line at 257.26 Å. We note that since the temperature and power-law tail parameters are free parameters of any electron distribution, diagnostics of the high-energy electrons always need to be performed simultaneously with diagnostics of temperature [60,72, and references therein].

3.3. Ion temperature and nonthermal diagnostics

Profiles of any emission line changes shape if energetic ions are present. This effect is detectable through the presence of enhanced line wings, which correspond to high-energy tails in ion velocity distribution via the Doppler effect. Such high-energy ions were detected in the last decade in a limited amount of cases, mostly in flares [62–65]. The most significant enhancements of the wings were found to occur at about twice the line FWHM [see Figure 1 of 64]. This means that in principle, any emission line with strong enough signal-to-noise in the far wings can be used for diagnostics of accelerated ions, independently of the temperature at which the line is formed. Thus, the wide temperature coverage of the solar corona provided by SISA fortuitously allows for wide diagnostics of energetic ions. However, the diagnostics are complicated by the fact that the emission lines are usually broadened during the impulsive phase of flares – a well known fact for decades [see Section 3.1 of [73] and also [63,65,74,75]. Since the broadening is indicative of the presence of turbulence, the wide spatial coverage of SISA shall enable the study of spatial correlations between the occurrence of turbulence and ion acceleration. We note that the two mechanisms can in principle be linked, with turbulence directly leading to particle acceleration in some cases [see, e.g., 76].

3.4. Electron Density Diagnostics

Measuring the electron density is a fundamental requirement for any spectrometer. Knowing the density is important for a wide range of issues, for example to estimate radiative losses of the plasma and thus the energy input required not only during flares, but also for the active region corona. In addition, electron density is critical for determining the ionization and recombination timescales in the plasma, and thus whether the plasma is in ionization equilibrium. The EUV offers a wide range of diagnostic possibilities, see the review by [69].

The SISA spectral range and sensitivity was also chosen to enable measurements of electron densities from a wide range of lines, formed from coronal (e.g. Fe IX, Fe XI, Fe XV, Ca XV) to flare temperatures (Fe XXI). Measurements of coronal densities have been carried out with previous spectrometers, most notably Hinode EIS, but measurements at high temperatures are nearly non-existent in the literature. The best diagnostics are in the soft X-rays around 140 Å, as discussed in [77], using lines mainly from Fe XXI and Fe XX. Such measurements have been carried out for a limited number of large X-class flares by [78] using SDO/EVE, an instrument without any spatial resolution. To estimate the ionization and recombination times of the flaring plasma, it is essential to measure the electron density at high temperatures with good spatial resolution. SISA has two excellent line ratios from Fe XXI. One is 242.05 Å /246.95 Å, which is sensitive to high densities, above 10^{12} cm^{-3}. The lines are strong and close. The other one is a ratio involving the weaker 178.9 Å line, which is sensitive already to active region densities of 10^{10} cm^{-3} or more. One issue with the 178.9 Å line is that it could be blended with a Ni XV line, depending on the relative amount of plasma at the formation

Preprints (www.preprints.org) | NOT PEER-REVIEWED | Posted: 29 November 2023 doi:10.20944/preprints202311.1854.v1

temperatures of these ions. To correct for the Ni XV blend, two other density-sensitive Ni XV lines need to be observed.

Figure 1 provides a summary of the main diagnostic ratios for SISA, although other ones are available. CHIANTI version 10 [79] was used. The ratios cover a wide range of temperatures and are sensitive to a wide range of densities. Note that the Fe IX ratio is the best density diagnostic for the solar corona, but has never been observed routinely. Also note that the Fe XXI ratio is one of the best ones across all wavelengths, to measure low electron densities which are expected to be present during the heating phase. Most other density diagnostics of flare lines, from the X-rays to the UV, are sensitive above 10^{12} cm^{-3}.

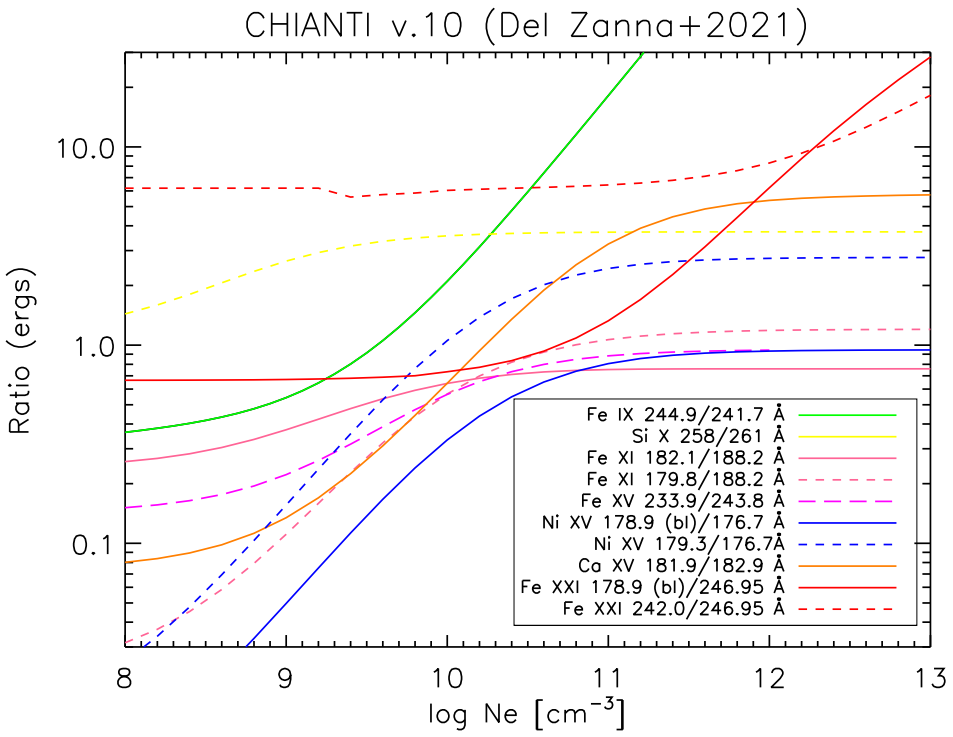

Figure 1. A selection of some important diagnostic spectral lines to measure electron densities.

3.5. Elemental Composition Diagnostics

Within the solar corona, there is a wide range of elemental abundances. As is the case for in-situ measurements, the variations are mainly associated with the First Ionization Potential (FIP) of the elements, indicating that the fractionation process that creates these variations occurs in the low chromosphere, where neutrals become ionized. The ratio of a low-FIP to a high-FIP element tend to be enhanced, compared to its photospheric value (the so-called FIP bias), although interesting cases of so-called inverse FIP effect have been observed. There is ample literature, but many earlier studies turned out to be incorrect, leading to a very confusing picture. A recent review of observational aspects is given in [69].

In a nutshell, the quiescent corona has nearly photospheric abundances, at least up to 1 MK; the hot 3 MK cores of active regions have an FIP bias of about 3–4; the cool active region loops have a wide range of FIP biases. Surges and flaring loops have been known since the Skylab time (1970's) to have photospheric abundances, interpreted as the indication that the plasma filling the loops evaporated from the chromosphere with a fast timescale such that the fractionation process did not occur. Interestingly, recent X-ray observations of small flares of GOES B-class have shown for the first time a rapid decrease of the FIP bias, followed by a gradual increase [80]. While the rapid decrease

 doi:10.20944/preprints202311.1854.v1

is expected to be caused by chromospheric evaporation, the gradual increase could be a signature of Alfvén waves.

There is general consensus that the FIP effect is related to the strength and topology of the magnetic field. A relatively simple hydrostatic model of the chromosphere put forward by M. Laming is able to explain the main features of the FIP effect and its inverse [see the review and references in 81]. The FIP effect would be caused by the ponderomotive force of trapped Alfven waves in magnetically-closed loops. Therefore, measuring the FIP effect and its variations during flares is important, as it could provide a way to indirectly confirm for the presence of Alfven waves or at least indicate the origin of the flaring plasma: if the flare loops have a FIP bias, then the plasma originated from closed loops already present in active regions.

The diagnostics to measure the relative abundances are limited, however, as there are only few ions formed at high temperatures from high-FIP elements. There are plenty of spectral lines from low-FIP elements such as Si, Fe, Mg, Ni, Ca instead. The best high-FIP ones, exploited in the 1970's and 1980's, are the H-like and He-like ions from oxygen, neon, argon and sulphur in the X-rays. Note that sulphur as a FIP of 10 eV, but in remote-sensing observations varies as the other high-FIP elements. Very few weak lines from high-FIP elements are present in the EUV and UV. A few very weak lines from Ar XIV and Ar XIII have been observed with Hinode EIS, which also has stronger S X, S XII and S XIII lines.

Across the whole EUV/UV, the best diagnostic lines are the strong Li-like doublets from Ar XVI at 353.8, 389.0 Å and from S XIV at 417.7, 445.7 Å. After them, the best diagnostic is the strongest (resonance) line from Ar XV at 221.15 Å, which is within the SISA spectral range. There are also interesting Ar XIV lines as the the strong 243.75 Å line, blended with Fe XV, or the 187.9 Å line, which becomes strong at high densities (but can also be blended), meaning that one would have to measure the density independently. Other good options within the SISA range are the strong S XIII at 256.6 Å and the lower-temperature S X lines, often used in previous Hinode EIS studies. Weak lines from Ar XIII are also available. There are plenty of lines from iron to be able to estimate the FIP bias measuring Ar/Fe and S/Fe in the 1–3 MK range.

3.6. Flare lines

There are several hot flare lines in the SISA spectral range. Close to Fe X 257.26 Å are the strong Fe XVII 254.9, Fe XXI 246.95 Fe XXII 247.19, 253.17, Ti XX 259.26, and Fe XXIV 255.1 Å lines. They span a temperature range $\log T = [6.6 - 7.3]$. Nearby, there is a strong Fe XXI line at 242.05Å which could be used in combination with the 246.95 (or the 187.9 Å) to measure densities above 10^{11} cm^{-3} (Section 3.4). This is an important diagnostic.

The strong Fe XXIII intercombination line is located at longer wavelengths, 263.76 Å. It would be an ideal electron temperature diagnostic in combination with the resonance line at 132 Å, if a second order could be observed.

Close to the 184.5 Å, there are several weaker hot lines, which become observable for large flares. Fe XXIII produces a line around 180. Å. There is a relatively strong Fe XXI line around 187.93 Å, however this line for weak flares is blended with an Ar XIV 187.96 Å line which is strongly density-sensitive, so careful deblending is needed. A weak Fe XXI around 178.9 Å is particularly important as it becomes strong at high electron densities, so it is one of the best density diagnostics for flare plasma, able to measure densities above 10^{10} cm^{-3}.

3.7. Departures from ionization equilibrium

Rapid heating or cooling of plasma can lead to departures from ionization equilibrium; a state when the plasma ionic composition does not reflect its electron temperature [e.g., 56,82–85]. This transient ionization in turn can affect other diagnostics [e.g., 86]. For a review of transient ionization conditions, see [59].

 doi:10.20944/preprints202311.1854.v1

Conditions favorable for occurrence of transient ionization are expected to arise in solar flares, where the energetic particles travel at fractions of the speed of light, and thus swiftly deposit large amounts of energy when encountering the dense solar chromosphere. This is so despite the electron densities ion flares are relatively high, leading to decrease of the timescales for collisional ionization and recombination [84], which are in flare plasma of the order of seconds or tens of seconds. Since the plasma evolves rapidly following the energy deposit, detecting transient ionization conditions requires fast cadence. Previous diagnostics of transient ionization [e.g., 82,83] focused on X-ray spectra, which were obtained with little or no spatial resolution and required scans across the wavelength range, while the detection of transient ionization from EUV was hampered by the twin problems of slit and throughput/cadence. For the first time, SISA will offer the spatial coverage, resolution, cadence, and lines from multiple ionization stages of iron (see Table 1), all required to detect signatures of transient ionization in rapidly evolving plasma along newly created flare loops.

3.8. Predicted signal in the main SISA lines

Given the previous requirements, namely provide spectral line diagnostics to measure magnetic fields, electron temperatures and densities, departures from ionization equilibrium in flaring plasma, non-Maxwellian electron distributions, variations in the FIP bias, and transient ionization, we designed a few possible multilayers to cover the key lines, as described below. Having selected one, we have then calculated the signal in the SISA lines.

As the target is to observe active regions and flares, two simulations have been carried out, one for the quiescent AR core, and one for an M2-class flare. For the AR core the predictions are based on an AR core loop observed by Hinode, see [87]. The Del Zanna (2013) coronal abundances are used, with an electron density of 2 $\times 10^9$ cm^{-3}. For the M2 flare the predictions are based on an M2-class flare observed by Hinode EIS. The Same set of abundances is used, but with electron density of 2 $\times 10^{10}$ cm^{-3}. In this case a full DEM analysis was carried out (Del Zanna et al. 2023, in prep). CHIANTI version 10 [79] was used. Table 1 shows the radiances of a few selected SISA lines and the corresponding data numbers per second per 1" pixel. It is clear that most lines are observable with exposures of 1 s.

4. Image slicer technology in the EUV regime

Among the Integral Field Unit (IFU) alternatives available to perform IFS, image slicers are the optimum for space: they are very compact with no moving mechanisms, lightweight, highly efficient and all parts are made of the same material.

As shown in Figure 2, an image slicer is an optical system composed typically of two or three arrays of mirrors, placed at the telescope's image focal plane. The first array (slicer mirror array) is composed of multiple narrow mirrors with a rectangular shape distributed such that the short dimension (width) corresponds to the spectral direction and the long dimension (length) is associated to the spatial direction. Each one of the slicer mirrors have a different tilt angle around the X and Y axes. Thus, each mirror reflects only a slice of the field of view, defined by its effective surface, in a different direction. The other arrays of mirrors are used to control the intermediate and exit pupils, re-image the slices of the field and reorganise them generating the spectrograph entrance slit. They can also produce a magnification, if required, enabling the perfect coupling between telescope and instrument, and adjusting the slit width to meet the desired resolution. Other advantages include no focal-ratio degradation and no polarisation effects.

Preprints (www.preprints.org) | NOT PEER-REVIEWED | Posted: 29 November 2023 doi:10.20944/preprints202311.1854.v1

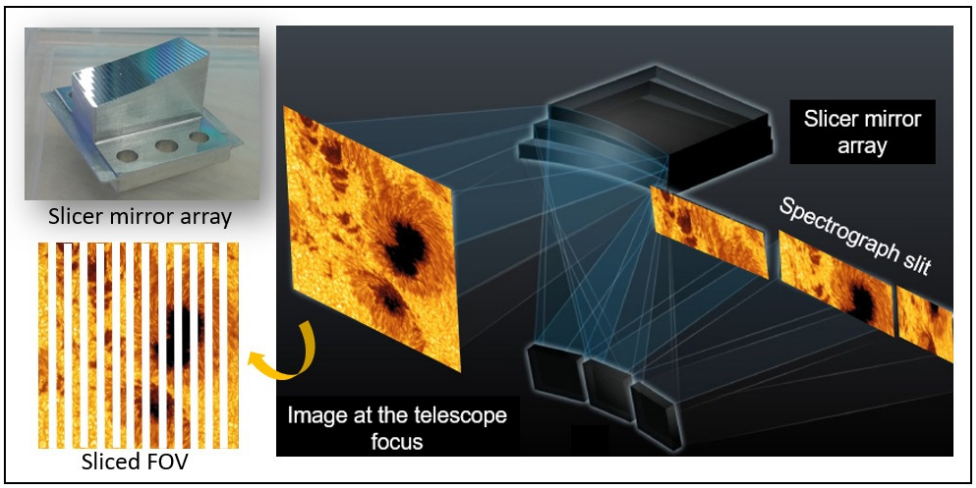

Figure 2. Conceptual sketch of an image slicer. The slicer mirror array divides the image generated by the telescope into slices that are re-imaged and reorganised by other mirror arrays, redistributing the 2D field of view into the spectrograph entrance slit.

Image slicers have been used for ground-based telescopes in the last few decades, operating at different spectral ranges from the infrared to UV/visible, for a wide variety of science cases. Some examples are shown in Figure 3 and include: VLT CUBES [88], BlueMUSE [89] and MUSE [90]; GTC FRIDA [91]; GNIRS [92] at Gemini North Telescope or ELT HARMONI [93] and METIS [94] for night-time observation. For solar physics, image slicers were first proposed for the integral field spectrograph [95,96] of the European Solar Telescope, which would observe in the optical. A prototype of this image slicer is operative at GREGOR solar telescope [97], which upgraded GRIS from a long-slit spectrograph to an integral field spectrograph, and observes in the infrared. No EUV solar IFS instrument has flown, though the SNIFS rocket mission, scheduled for a 2024 launch, will observe solar Ly α using IFS [3].

There are also spaceborne image slicers on-board the James Webb Space Telescope in NIRSpec [98] and MIRI [99] operating at infrared wavelengths. At much shorter wavelengths, INFUSE [100] was the first IFS in the Far Ultraviolet (FUV), while SISA [101] will be the first IFS in the Extreme Ultraviolet, applying the image slicer technology at the shortest wavelengths ever proposed.

Finally, a different approach to the 2D coverage problem has been adopted by the Multi-slit Solar Explorer [102–104, MUSE;], a NASA Heliophysics Medium-class Explorer with scheduled launch in 2027. Thanks to its 35-slit design, MUSE will provide high-cadence (<20 s or faster for flares), sub-arcsecond resolution spectroscopic rasters over an active region size, targeting 4 isolated, strong spectral lines (Fe IX 171 Å at 0.7 MK, Fe XV 284 Å at 2 MK, Fe XIX at 108 Å at 10 MK, and Fe XXI 108 Å at 12 MK). With its unique capabilities, MUSE will provide new crucial discoveries for flare science [104]. SISA would build upon the science legacy of MUSE by providing high-cadence 2D imaging from a larger set of spectral lines that offer rich diagnostic potential.

Preprints (www.preprints.org) | NOT PEER-REVIEWED | Posted: 29 November 2023 doi:10.20944/preprints202311.1854.v1

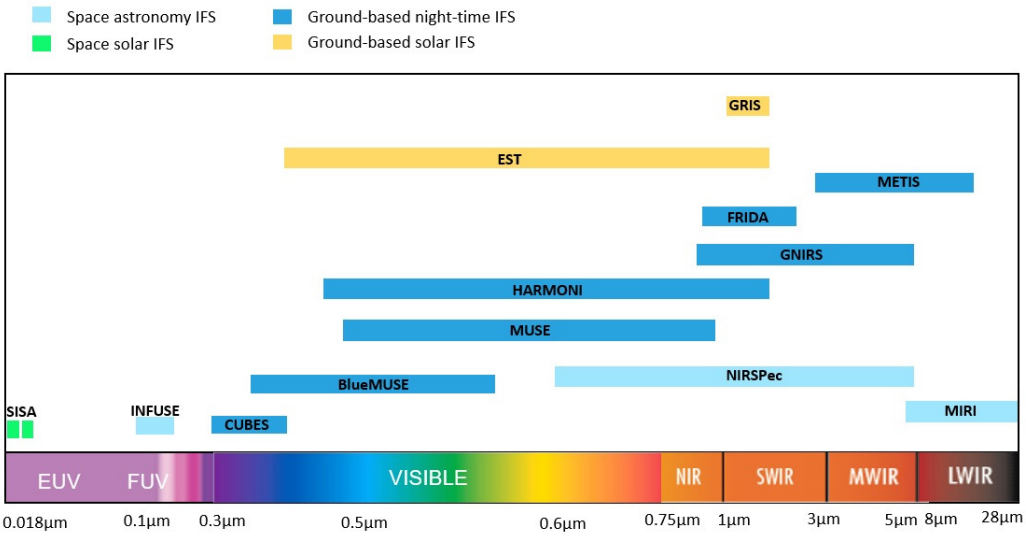

Figure 3. SISA will break new ground both technologically by observing using image slicers in the EUV, and scientifically by providing high cadence 2D spectra of various solar phenomenon. Currently operating image slicers based IFS operating at different spectral ranges for solar and night-time ground-based telescopes and space missions observe at longer wavelengths than SISA.

At the shorter wavelengths of the EUV regime that SISA will explore, the application of image slicers presents additional challenges [101], like: narrower slicer mirrors for high resolution solar observations, surface roughness, and coating. A slicer width of 15 μm has been defined for SISA, which is narrower than the slicer mirror width that is currently achievable both for glass and metallic slicer mirrors. This width is even more difficult to achieve on curved substrates (powered slicer mirrors), whose use would enable the reduction of the number of optical components to maximise throughput. At these short wavelengths the surface roughness is a key factor to minimise stray light that could potentially compromise the instrument sensitivity.

These technological challenges of the image slicer technology for the EUV are being addressed and developed in the UK by a collaboration between Durham University and University College London (UCL) within two on-going projects: MINOS and LUCES. MINOS (Manufacturing of Image slicer Novel technology for Space), funded by Durham University, explores the state-of-the-art of glass slicers producing a slicer demonstrator with the thinnest width currently achievable on spherical substrates of 70 μm and enhanced surface roughness below 1 nm RMS. This demonstrator is being manufactured by Bertin Winlight, in France.

LUCES (Looking Up image slicers optimum Capabilities in the EUV for Space) is funded by the Enabling Technology Programme of the UK Space Agency and will produce multiple powered slicer mirror demonstrators in metal using different widths to determine the narrowest achievable width with diamond machining techniques at Durham University, and on different substrate to compare surface roughness. These projects will increase the technology readiness level (TRL) of the image slicer technology for EUV applications.

5. SISA instrument proposal

5.1. Specifications

The Spectral Imager of the Solar Atmosphere (SISA) is the first EUV imaging spectrometer using image slicer technology in the $\lambda = [180 - 260]$ Å range. SISA will observe a threshold field of view (FoV) of $100'' \times 100''$ (with a goal of $100'' \times 250''$), obtaining spectra of the whole 2D field of view in

Preprints (www.preprints.org) | NOT PEER-REVIEWED | Posted: 29 November 2023 doi:10.20944/preprints202311.1854.v1

less than 3 seconds for high signal objects (e.g. flares) and less than 30 seconds for low signal ones. This field of view will be observed in two spectral windows simultaneously, Window 1 $\lambda = [178 - 184]$ Å, and Window 2 $\lambda = [246 - 258]$ Å, with a spectral resolving power (R) of $R = [3560 - 5160]$, a spatial resolution of $< 3''$, and a spectral resolution of 0.05 Å Full Width at Half Maximum (FWHM).

The defined spatial resolution is required to satisfactorily resolve flare loops and ribbon/footpoint sources, including newly reconnected ones, whilst the spectral resolution is required to resolve the main diagnostic lines and measure nonthermal line profiles. The FoV of $100'' \times 100''$ can capture the core of large X-class flares, the entirety of smaller flares, or a portion of an active region. A high signal temporal resolution (Cadence 1) of 3 s will capture much of the dynamics of many flares, whilst being two orders of magnitude faster than previously observed for 2D EUV imaging spectroscopy. A low signal temporal resolution (Cadence 2) of 30 seconds will capture the slower dynamics present in the active regions or quiet Sun areas.

The two spectral ranges are required to measure the parameters of both 1 MK plasma and the much hotter 15 MK plasma that appears during flares, and include lines sensitive to the coronal magnetic field strength, electron temperature/non-Maxwellian electron distributions, a wide range of lines to measure electron densities from coronal (e.g. Fe IX, Fe XI, Fe XII, Fe XV, Ca XV) to flare temperatures (Fe XXI), and the FIP bias. The specifications for SISA are presented in Table 2.

Table 2. Specifications for the instrument SISA.

Field of View	$100'' \times 100''$
Spectral Window 1	$178 - 184$ Å
Spectral Window 2	$246 - 258$ Å
Spectral resolution	0.05 Å FWHM
Spatial resolution	$< 3''$
Spectral Resolving Power (R)	$3560 - 5160$
Temporal resolution (high signal)	< 3 seconds
Temporal resolution (low signal)	< 30 seconds

5.2. Layout

The solar EUV photon flux is very low, demanding a sensitive instrument. SISA combines the surfaces of the Integral Field Unit (IFU) with those of the spectrograph in a compact and highly efficient layout that uses only an array of powered slicer mirrors and an array of curved diffraction gratings as shown in Figure 4. This layout is based on a design presented by Calcines et al. 2018 [105] for applications for ultra-compact integral field spectrograph and is inspired in IGIS [106], which first proposed the combination of the IFU and the spectrograph components. SISA does not have an entrance slit, it covers a 2D field of view without any scanning mechanisms obtaining all spectra of a 2D region of the Sun within one exposure.

Two subsystems are identified: the telescope and the integral field spectrograph, with a total of three surfaces. To optimise efficiency, the telescope is composed of one off-axis parabolic mirror, with an aperture of 200 mm diameter and an effective focal length of 3 metres. At its focal plane, the array of slicer mirrors, each one of them with different orientations, divide the image of the field into thin slices of 15 μm. To cover a field of view of $100'' \times 100''$, a hundred slicer mirrors are needed, with rectangular shape and whose dimensions are 3.64 mm length by 15 μm width. The slicer mirror array decomposes the incoming beam into as many sub-beams as the number of slicer mirrors, generating a pupil for each one of them. At the pupil position an array of curved gratings will disperse the light and focus the beams at their focal length. Each grating will produce the spectrum associated with a slice of the field. The different orientations for the gratings are defined to distribute the spectra on the detectors. These orientations are fixed, with no moving mechanisms.

Preprints (www.preprints.org) | NOT PEER-REVIEWED | Posted: 29 November 2023 doi:10.20944/preprints202311.1854.v1

The design of SISA includes different trade-off analyses, such as the definition of the telescope effective focal length versus resolution and slicer mirror width. For the dispersive element, two options were considered: a larger diffraction grating versus an array of gratings, one per slice. Whilst a larger grating would provide higher spectral resolving power, curved gratings present aberrations for off-axis fields. The use of an array facilitates the organisation of the spectra on the detectors. This is currently the selected option.

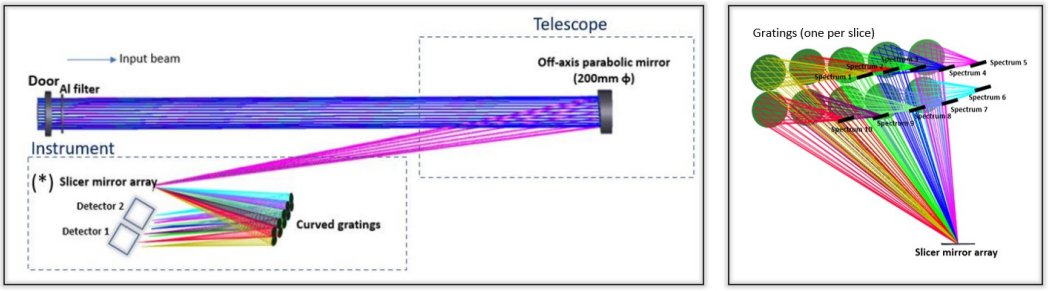

Figure 4. SISA's conceptual layout (left) and view of the spectra per slice generated by each curved grating (right).

5.3. Components

As mentioned in the previous section, SISA is composed of two subsystems: (1) the telescope and (2) the instrument. A door protection mechanism will be installed at the front of the instrument. This door will be used to provide safety against acoustic vibration and venting during the launch. It will also protect the instrument from contamination during assembly, integration and verification (AIV), launch and in-orbit, and control the venting and reduce air flow during on-ground purging and launch. CSL is considered as the future supplier for the door based on their previous experience designing the door for the Extreme Ultraviolet Imager (EUI) onboard Solar Orbiter.

The aperture of the telescope (200 mm) was selected to optimise throughput with respect to existing EUV instruments. The same supplier of the METIS/Solar Orbiter mirrors is considered, TOPTEC, Institute of Plasma Physics of the Czech Academy of Sciences with TRL 9. The manufacturing feasibility of mirrors with apertures up to 300 mm has been confirmed.

The slicer mirror technology presents technology readiness level (TRL) 9 in the infrared. For the EUV this technology is currently under development. MINOS and LUCES projects will raise the TRL in the EUV to TRL 4. Although the slicers are the component with the lowest TRL for this spectral range, its application is a game-changer for EUV solar spectroscopy. The on-going developments within the UK in this field, together with a plan in place to achieve TRL 6 within the next several years will enable this technology to be considered for the next generation of solar space missions.

Curved holographic gratings have already been used for other instruments like EIS and the upcoming EUV High-Throughput Spectroscopic Telescope [EUVST 107], with TRL 9. For the gratings for SISA, IAS in France is currently considered as the future lead institution. The possibility of using metallic curved gratings made on the same material as the slicer mirrors will also be investigated.

The SISA instrument requires a large-size image sensor with high EUV sensitivity. The baseline will be to use back-illuminated CMOS radiation-hardened active-pixel image sensor (APS), developed by CSL/ROB (Belgium). Compared to CCD technology, CMOS-APS detectors do not require a mechanical shutter, have a greater radiation tolerance (low charge transfer), low power consumption, high speed and dynamic range, with non destructive readout for low readout noise. Additional features include random addressing, windowing and anti-blooming. SISA's detectors must be cooled to a temperature lower than -40 C (ideally around -60 C), with a stability of $\pm$ 5 C.

Preprints (www.preprints.org) | NOT PEER-REVIEWED | Posted: 29 November 2023 doi:10.20944/preprints202311.1854.v1

5.4. Efficiency

The efficiency of the instrument will be limited by two important factors: (1) the possibility of using only two optical components for the integral field spectrograph and only one for the telescope based on the performance on optical quality and (2) the coating.

For the simultaneous observation of the two spectral windows, a dual-band multi-layer coating is being designed for SISA at the National Research Council of Italy, Padova. Considering the required operational spectral bands for SISA, the most efficient coatings in terms of efficiency were identified to be the three-material multilayer Al/Mo/B_4C or, alternatively, the Al/Mo/SiC [108]. Both coatings show very good long-term stability, and in the case of Al/Mo/SiC its reliability has been proven through its successful use in the *Solar Orbiter*/EUI instrument. The multiband response required for SISA was obtained by using a design consisting of a superposition of two periodic multilayer stacks separated by two or three buffer layers. The coatings optimization was performed by using a genetic algorithm, following the procedure previously described in [109]. Figure 5 shows the three options obtained with an Al/Mo/B_4C multilayer, among which Option 3 is the preferred alternative due to it offering the broadest response, with signal near 220 Å. Similar results can be obtained with the Al/Mo/SiC multilayer.

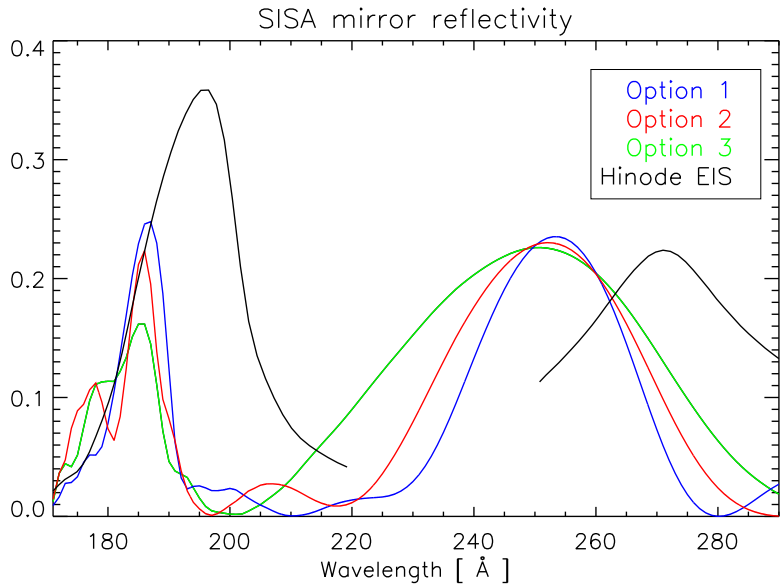

Figure 5. Reflectivities for the three multi-layer coatings under design for SISA.

A preliminary estimation of the throughput has been performed. The effective area for SISA is represented in Figure 6 (in black), compared to *Hinode*/EIS (in blue). To calculate the effective area we have considered the following components: (1) a front Al filter, the same used for SDO/AIA, but with an improved mesh transmission of 95%, compared to the AIA one (85%). Such improved mesh has already flown on the Hi-C sounding rockets. The AIA filters have shown little degradation at the SISA wavelengths, probably thanks to their carbon layer, but alternative coatings will be considered. (2) Two mirror reflectivities (one for the primary, one for the slicer mirrors) using the multilayer option 3; (3) A third reflectivity using the same multilayer for the grating, with an efficiency of 35%, the same measured for the Hinode EIS grating in the long wavelength channel; and (4) The same quantum efficiency of the EIS CCD, 0.85. A secondary focal plane filter has not been included to maximise throughput, although a rotating wheel of redundant focal plane filters should be included.

The significant improvement over the EIS effective areas is due to the slightly larger aperture (20 cm instead of 15), and the fact that a single multilayer is used (the EIS aperture is sectioned with two

Preprints (www.preprints.org) | NOT PEER-REVIEWED | Posted: 29 November 2023 doi:10.20944/preprints202311.1854.v1

different multilayers). Also, the multilayer has been designed to have maximum reflectance close to the main diagnostic lines around 250 Å.

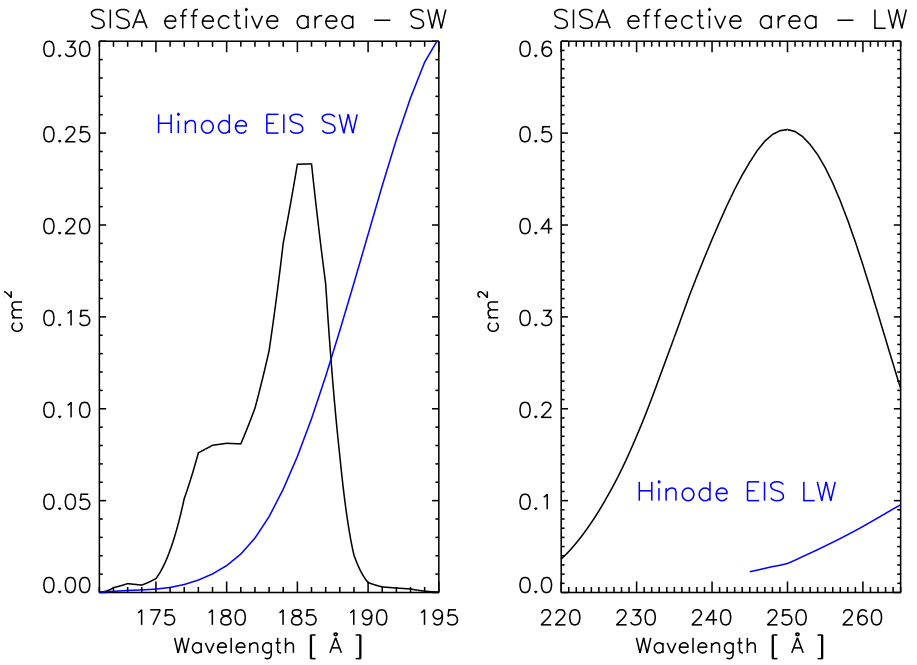

Figure 6. Preliminary esimates of SISA's effective area (black), compared to *Hinode*/EIS' short wavelength (SW) and long wavelength (LW) channels (blue).

6. Conclusions

Integral Field Spectroscopy is one of the most powerful techniques applied in astronomy. The ability to obtain the spectra of a 2D field of view simultaneously reduces the integration time by over two orders of magnitude. Despite this great advantage, this technique has not been used in the Extreme Ultraviolet regime, which can only be observed from space, due to the limitations and challenges for the existing Integral Field Unit alternatives. The image slicer technology seems to be the optimum choice, offering a compact, robust, highly efficient solution with no moving mechanisms. The SPARK (Solar Particle Acceleration Radiation and Kinetics) mission proposal led by the UK (UCL) includes the first ever integral field spectrograph in the EUV: SISA. SISA consists of a three mirror system including the telescope and the instrument.

A preliminary study has identified optimal spectral ranges to allow many plasma diagnostics, some of which are not available to current (Hinode EIS) or future EUV instruments (EUVST, MUSE). With a relatively small aperture of 20 cm diameter, a single multilayer and the slicers, we expect to perform the types of measurements that Hinode EIS has been producing about 100 times faster.

Although the image slicer technology currently presents low TRL at EUV wavelengths, the UK (Durham University and UCL) have some on-going research and development projects that will soon enable this technology for the next generation of space missions, including solar physics and all fields of astronomy.

SISA, currently under design study, promises to be a game changer in our understanding of our star, the Sun.

Author Contributions: The paper writing was led by Ariadna Calcines. The paper was based upon the SPARK mission concept that was coordinated by Hamish A. S. Reid, Sophie Musset and Daniel F. Ryan. All other authors contributed by providing scientific expertise or instrumentation expertise in the development of the SISA instrument concept and/or the paper itself. The selection of the SISA diagnostic lines in Table 1 was led by G.D.Z. All authors have read and agreed to the published version of the manuscript.

 doi:10.20944/preprints202311.1854.v1

Funding: HASR and SAM were funded by the UK Science, Technology and Facilities Council (STFC) under the consolidated grant ST/W001004/1. GDZ acknowledges support from STFC via the consolidated grants to the atomic astrophysics group at DAMTP, University of Cambridge (ST/P000665/1. and ST/T000481/1). JD acknowledges the Czech National Science Foundation, Grant No. GACR 22-07155S, as well as institutional support RWO:67985815 from the Czech Academy of Sciences. GSK acknowledges financial support from NASA's Early Career Investigator Program (Grant# NASA 80NSSC21K0460). DOS acknowledges financial support from the grants AEI/MCIN/10.13039/501100011033/(RTI2018-096886-C5, PID2021-125325OB-C5, PCI2022-135009-2) and ERDF "A way of making Europe" and "Center of Excellence Severo Ochoa" award to IAA-CSIC (CEX2021-001131-S). LAH is supported by an ESA Research Fellowship.

Data Availability Statement: No new data were created or analyzed in this study. Data sharing is not applicable 527 to this article.

Acknowledgments: JD wishes to acknowledge useful discussions with E. Dzifčáková.

Conflicts of Interest: The authors declare no conflict of interest.

Abbreviations

The following abbreviations are used in this manuscript:

AIV	Alignment Integration and Verification
CCD	Charge-coupled Device
CME	Coronal Mass Ejection
CUBES	Cassegrain U-Band Efficient Spectrograph
EIS	EUV Imaging Spectrometer onboard Hinode
ELT	Extremely Large Telescope
EUV	Extreme Ultraviolet
EUVST	Extreme Ultraviolet High-Throughput Spectroscopic Telescope
EVE	EUV Variability Experiment onboard SDO
FIP	First Ionisation Potential
FOXSI	Focusing Optics X-ray Solar Imager
FRIDA	inFRared Imager and Dissector for Adaptive optics
Full Width Half Maximum	
FUV	Far Ultraviolet
FWHM	Full Width Half Maximum
GOES	Geostationary Operational Environmental Satellite
GNIRS	Gemini Near-InfraRed Spectrograph
GRIS	Gregor Infrared Spectrograph
GTC	Gran Telescopio Canarias
HARMONI	High Angular Resolution Monolithic Optical and Near-infrared Integral field spectrograph
HXR	Hard X-ray
IFS	Integral Field Spectrograph
IFU	Integral Field Unit
INFUSE	INtegral Field Ultraviolet Spectroscopic Experiment
LISSAN	Large Imaging Spectrometer for Solar Accelerated Nuclei
LUCES	Looking Up image slicer optimum Capabilities in the EUV for Space
METIS	Mid-Infrared E-ELT Imager and Spectrograph
MHD	Magnetohydrodynamic
MINOS	Manufacturing of Image slicer NOvel technology for Space
MIRI	Mid-Infrared Instrument
MUSE	Multi-Slit Solar Explorer
QPP	Quasi-Periodic Pulsations
SDO	Solar Dynamics Observatory
SISA	Spectral Imager of the Solar Atmosphere
SNIFS	Solar eruptioN Integral Field Spectrograph
SPARK	Solar Particle Acceleration, Radiation and Kinetics mission
SXR	Soft X-ray
TRL	Technology Readiness Level

References

1. Culhane, J.L.; Harra, L.K.; James, A.M.; Al-Janabi, K.; Bradley, L.J.; Chaudry, R.A.; Rees, K.; Tandy, J.A.; Thomas, P.; Whillock, M.C.R.; et al. The EUV Imaging Spectrometer for Hinode. *Sol Phys* **2007**, *243*, 19–61. https://doi.org/10.1007/s01007-007-0293-1.
2. De Pontieu, B.; Title, A.M.; Lemen, J.R.; Kushner, G.D.; Akin, D.J.; Allard, B.; Berger, T.; Boerner, P.; Cheung, M.; Chou, C.; et al. The Interface Region Imaging Spectrograph (IRIS). *Sol Phys* **2014**, *289*, 2733–2779, [arXiv:astro-ph.SR/1401.2491]. https://doi.org/10.1007/s11207-014-0485-y.
3. Chamberlin, P.C.; Schmit, D.J.; Daw, A.N.; Polito, V.; Gong, Q.; Milligan, R.O. The Solar eruptioN Integral Field Spectrograph (SNIFS) Sounding Rocket. In Proceedings of the AGU Fall Meeting Abstracts, 2020, Vol. 2020, pp. SH056–03.
4. Knoer, V.; Chamberlin, P.; Daw, A.; Gong, Q.; Milligan, R.; Polito, V.; Schmit, D. A Novel Integral Field Spectrograph Design for taking High-Cadence Spectral Solar Images: SNIFS. In Proceedings of the AGU Fall Meeting Abstracts, 2021, Vol. 2021, pp. SH55B–1837.
5. Young, P.R.; Doschek, G.A.; Warren, H.P.; Hara, H. Properties of a Solar Flare Kernel Observed by Hinode and SDO. *ApJ* **2013**, *766*, 127, [arXiv:astro-ph.SR/1212.4388]. https://doi.org/10.1088/0004-637X/766/2/127.
6. Polito, V.; Reep, J.W.; Reeves, K.K.; Simões, P.J.A.; Dudík, J.; Del Zanna, G.; Mason, H.E.; Golub, L. Simultaneous IRIS and Hinode/EIS Observations and Modelling of the 2014 October 27 X2.0 Class Flare. *ApJ* **2016**, *816*, 89, [arXiv:astro-ph.SR/1512.06378]. https://doi.org/10.3847/0004-637X/816/2/89.
7. Panos, B.; Kleint, L.; Huwyler, C.; Krucker, S.; Melchior, M.; Ullmann, D.; Voloshynovskiy, S. Identifying Typical Mg II Flare Spectra Using Machine Learning. *ApJ* **2018**, *861*, 62, [arXiv:astro-ph.SR/1805.10494]. https://doi.org/10.3847/1538-4357/aac779.
8. Polito, V.; Kerr, G.S.; Xu, Y.; Sadykov, V.M.; Lorincik, J. Solar Flare Ribbon Fronts. I. Constraining Flare Energy Deposition with IRIS Spectroscopy. *ApJ* **2023**, *944*, 104, [arXiv:astro-ph.SR/2211.05333]. https://doi.org/10.3847/1538-4357/acaf7c.
9. Qiu, J.; Lee, J.; Gary, D.E.; Wang, H. Motion of Flare Footpoint Emission and Inferred Electric Field in Reconnecting Current Sheets. *ApJ* **2002**, *565*, 1335–1347. https://doi.org/10.1086/324706.
10. Fletcher, L.; Pollock, J.A.; Potts, H.E. Tracking of TRACE Ultraviolet Flare Footpoints. *Sol Phys* **2004**, *222*, 279–298. https://doi.org/10.1023/B:SOLA.0000043580.89730.4d.
11. Sun, X.; Hoeksema, J.T.; Liu, Y.; Aulanier, G.; Su, Y.; Hannah, I.G.; Hock, R.A. Hot Spine Loops and the Nature of a Late-phase Solar Flare. *ApJ* **2013**, *778*, 139, [arXiv:astro-ph.SR/1310.1438]. https://doi.org/10.1088/0004-637X/778/2/139.
12. Dudík, J.; Janvier, M.; Aulanier, G.; Del Zanna, G.; Karlický, M.; Mason, H.E.; Schmieder, B. Slipping Magnetic Reconnection during an X-class Solar Flare Observed by SDO/AIA. *ApJ* **2014**, *784*, 144, [arXiv:astro-ph.SR/1401.7529]. https://doi.org/10.1088/0004-637X/784/2/144.
13. Dudík, J.; Polito, V.; Janvier, M.; Mulay, S.M.; Karlický, M.; Aulanier, G.; Del Zanna, G.; Dzifčáková, E.; Mason, H.E.; Schmieder, B. Slipping Magnetic Reconnection, Chromospheric Evaporation, Implosion, and Precursors in the 2014 September 10 X1.6-Class Solar Flare. *ApJ* **2016**, *823*, 41, [arXiv:astro-ph.SR/1603.06092]. https://doi.org/10.3847/0004-637X/823/1/41.
14. Li, T.; Zhang, J. Slipping Magnetic Reconnection Triggering a Solar Eruption of a Triangle-shaped Flag Flux Rope. *ApJL* **2014**, *791*, L13, [arXiv:astro-ph.SR/1407.4180]. https://doi.org/10.1088/2041-8205/791/1/L13.
15. Li, T.; Zhang, J. Quasi-periodic Slipping Magnetic Reconnection During an X-class Solar Flare Observed by the Solar Dynamics Observatory and Interface Region Imaging Spectrograph. *ApJL* **2015**, *804*, L8, [arXiv:astro-ph.SR/1504.01111]. https://doi.org/10.1088/2041-8205/804/1/L8.
16. Sobotka, M.; Dudík, J.; Denker, C.; Balthasar, H.; Jurčák, J.; Liu, W.; Berkefeld, T.; Collados Vera, M.; Feller, A.; Hofmann, A.; et al. Slipping reconnection in a solar flare observed in high resolution with the GREGOR solar telescope. *A&A* **2016**, *596*, A1, [arXiv:astro-ph.SR/1605.00464]. https://doi.org/10.1051/0004-6361/201527966.
17. Lörinčík, J.; Aulanier, G.; Dudík, J.; Zemanová, A.; Dzifčáková, E. Velocities of Flare Kernels and the Mapping Norm of Field Line Connectivity. *ApJ* **2019**, *881*, 68, [arXiv:astro-ph.SR/1906.01880]. https://doi.org/10.3847/1538-4357/ab298f.
18. Lörinčík, J.; Dudík, J.; Polito, V. Blueshifted Si IV 1402.77 Å Line Profiles in a Moving Flare Kernel Observed by IRIS. *ApJ* **2022**, *934*, 80. https://doi.org/10.3847/1538-4357/ac78e2.

19. Aulanier, G.; Pariat, E.; Démoulin, P.; Devore, C.R. Slip-Running Reconnection in Quasi-Separatrix Layers. *Sol Phys* **2006**, *238*, 347–376. https://doi.org/10.1007/s11207-006-0230-2.
20. Aulanier, G.; Janvier, M.; Schmieder, B. The standard flare model in three dimensions. I. Strong-to-weak shear transition in post-flare loops. *A&A* **2012**, *543*, A110. https://doi.org/10.1051/0004-6361/201219311.
21. Janvier, M.; Aulanier, G.; Pariat, E.; Démoulin, P. The standard flare model in three dimensions. III. Slip-running reconnection properties. *A&A* **2013**, *555*, A77, [arXiv:astro-ph.SR/1305.4053]. https://doi.org/10.1051/0004-6361/201321164.
22. De Pontieu, B.; Polito, V.; Hansteen, V.; Testa, P.; Reeves, K.K.; Antolin, P.; Nóbrega-Siverio, D.E.; Kowalski, A.F.; Martinez-Sykora, J.; Carlsson, M.; et al. A New View of the Solar Interface Region from the Interface Region Imaging Spectrograph (IRIS). *Sol Phys* **2021**, *296*, 84, [arXiv:astro-ph.SR/2103.16109]. https://doi.org/10.1007/s11207-021-01826-0.
23. Kerr, G.S. Interrogating Solar Flare Loop Models with IRIS Observations 1: Overview of the Models, and Mass flows. *Frontiers in Astronomy and Space Sciences* **2022**, *9*, 1060856, [arXiv:astro-ph.SR/2212.06647]. https://doi.org/10.3389/fspas.2022.1060856.
24. Kerr, G.S. Interrogating Solar Flare Loop Models with IRIS Observations 2: Plasma Properties, Energy Transport, and Future Directions. *Frontiers in Astronomy and Space Sciences* **2023**, *9*, 1060862, [arXiv:astro-ph.SR/2212.06261]. https://doi.org/10.3389/fspas.2022.1060862.
25. Allred, J.C.; Kerr, G.S.; Gordon Emslie, A. Solar Flare Heating with Turbulent Suppression of Thermal Conduction. *ApJ* **2022**, *931*, 60, [arXiv:astro-ph.SR/2204.11684]. https://doi.org/10.3847/1538-4357/ac69e8.
26. Cheung, M.C.M.; Martínez-Sykora, J.; Testa, P.; De Pontieu, B.; Chintzoglou, G.; Rempel, M.; Polito, V.; Kerr, G.S.; Reeves, K.K.; Fletcher, L.; et al. Probing the Physics of the Solar Atmosphere with the Multi-slit Solar Explorer (MUSE). II. Flares and Eruptions. *ApJ* **2022**, *926*, 53, [arXiv:astro-ph.SR/2106.15591]. https://doi.org/10.3847/1538-4357/ac4223.
27. Ashfield, W.; Longcope, D. A Model for Gradual-phase Heating Driven by MHD Turbulence in Solar Flares. *ApJ* **2023**, *944*, 147, [arXiv:astro-ph.SR/2301.04592]. https://doi.org/10.3847/1538-4357/acb1b2.
28. Nakariakov, V.M.; Melnikov, V.F. Quasi-Periodic Pulsations in Solar Flares. *Space Sci. Rev.* **2009**, *149*, 119–151. https://doi.org/10.1007/s11214-009-9536-3.
29. McLaughlin, J.A.; Nakariakov, V.M.; Dominique, M.; Jelínek, P.; Takasao, S. Modelling Quasi-Periodic Pulsations in Solar and Stellar Flares. *Space Sci. Rev.* **2018**, *214*, 45, [arXiv:astro-ph.SR/1802.04180]. https://doi.org/10.1007/s11214-018-0478-5.
30. Zimovets, I.V.; McLaughlin, J.A.; Srivastava, A.K.; Kolotkov, D.Y.; Kuznetsov, A.A.; Kupriyanova, E.G.; Cho, I.H.; Inglis, A.R.; Reale, F.; Pascoe, D.J.; et al. Quasi-Periodic Pulsations in Solar and Stellar Flares: A Review of Underpinning Physical Mechanisms and Their Predicted Observational Signatures. *Space Sci. Rev.* **2021**, *217*, 66. https://doi.org/10.1007/s11214-021-00840-9.
31. Clarke, B.P.; Hayes, L.A.; Gallagher, P.T.; Maloney, S.A.; Carley, E.P. Quasi-periodic Particle Acceleration in a Solar Flare. *ApJ* **2021**, *910*, 123, [arXiv:astro-ph.SR/2102.04267]. https://doi.org/10.3847/1538-4357/abe463.
32. Hayes, L.A.; Inglis, A.R.; Christe, S.; Dennis, B.; Gallagher, P.T. Statistical Study of GOES X-Ray Quasi-periodic Pulsations in Solar Flares. *ApJ* **2020**, *895*, 50, [arXiv:astro-ph.SR/2004.11775]. https://doi.org/10.3847/1538-4357/ab8d40.
33. Nakariakov, V.M.; Foullon, C.; Myagkova, I.N.; Inglis, A.R. Quasi-Periodic Pulsations in the Gamma-Ray Emission of a Solar Flare. In Proceedings of the EGU General Assembly Conference Abstracts, 2010, EGU General Assembly Conference Abstracts, p. 8615.
34. Brosius, J.W.; Daw, A.N.; Inglis, A.R. Quasi-periodic Fluctuations and Chromospheric Evaporation in a Solar Flare Ribbon Observed by Hinode/EIS, IRIS, and RHESSI. *ApJ* **2016**, *830*, 101. https://doi.org/10.3847/0004-637X/830/2/101.
35. Mishra, S.K.; Sangal, K.; Kayshap, P.; Jelínek, P.; Srivastava, A.K.; Rajaguru, S.P. Origin of Quasi-periodic Pulsation at the Base of a Kink-unstable Jet. *ApJ* **2023**, *945*, 113, [arXiv:astro-ph.SR/2301.01534]. https://doi.org/10.3847/1538-4357/acb058.
36. Xu, J.; Ning, Z.; Li, D.; Shi, F. Quasi-Periodic Pulsations in an M-Class Solar Flare. *Universe* **2023**, *9*, 215. https://doi.org/10.3390/universe9050215.
37. Emslie, A.G.; Sturrock, P.A. Temperature minimum heating in solar flares by resistive dissipation of Alfvén waves. *Sol Phys* **1982**, *80*, 99–112. https://doi.org/10.1007/BF00153426.

38. Fletcher, L.; Hudson, H.S. Impulsive Phase Flare Energy Transport by Large-Scale Alfvén Waves and the Electron Acceleration Problem. *ApJ* **2008**, *675*, 1645–1655, [0712.3452]. https://doi.org/10.1086/527044.
39. Russell, A.J.B.; Fletcher, L. Propagation of Alfvénic Waves from Corona to Chromosphere and Consequences for Solar Flares. *ApJ* **2013**, *765*, 81, [arXiv:astro-ph.SR/1302.2458]. https://doi.org/10.1088/0004-637X/765/2/81.
40. Reep, J.W.; Russell, A.J.B. Alfv\'enic Wave Heating of the Upper Chromosphere in Flares. *ApJL* **2016**, *818*, L20, [arXiv:astro-ph.SR/1601.01969]. https://doi.org/10.3847/2041-8205/818/1/L20.
41. Reep, J.W.; Russell, A.J.B.; Tarr, L.A.; Leake, J.E. A Hydrodynamic Model of Alfvénic Wave Heating in a Coronal Loop and Its Chromospheric Footpoints. *ApJ* **2018**, *853*, 101, [arXiv:astro-ph.SR/1712.06171]. https://doi.org/10.3847/1538-4357/aaa2fe.
42. Kerr, G.S.; Fletcher, L.; Russell, A.J.B.; Allred, J.C. Simulations of the Mg II k and Ca II 8542 lines from an AlfvÉn Wave-heated Flare Chromosphere. *ApJ* **2016**, *827*, 101, [arXiv:astro-ph.SR/1605.05888]. https://doi.org/10.3847/0004-637X/827/2/101.
43. Chifor, C.; Tripathi, D.; Mason, H.E.; Dennis, B.R. X-ray precursors to flares and filament eruptions. *A&A* **2007**, *472*, 967–979. https://doi.org/10.1051/0004-6361:20077771.
44. Hudson, H.; Fletcher, L.; Hannah, I.; Hayes, L.; Simoes, P. Hot onsets of solar flares. In Proceedings of the AGU Fall Meeting Abstracts, 2021, Vol. 2021, pp. SH22B–02.
45. Cargill, P.J. Active Region Emission Measure Distributions and Implications for Nanoflare Heating. *ApJ* **2014**, *784*, 49. https://doi.org/10.1088/0004-637X/784/1/49.
46. Klimchuk, J.A. Key aspects of coronal heating. *Philosophical Transactions of the Royal Society of London Series A* **2015**, *373*, 20140256–20140256, [arXiv:astro-ph.SR/1410.5660]. https://doi.org/10.1098/rsta.2014.0256.
47. Schmelz, J.T.; Winebarger, A.R. What can observations tell us about coronal heating? *Philosophical Transactions of the Royal Society of London Series A* **2015**, *373*, 20140257–20140257. https://doi.org/10.1098/rsta.2014.0257.
48. Warren, H.P.; Reep, J.W.; Crump, N.A.; Ugarte-Urra, I.; Brooks, D.H.; Winebarger, A.R.; Savage, S.; De Pontieu, B.; Peter, H.; Cirtain, J.W.; et al. Observation and Modeling of High-temperature Solar Active Region Emission during the High-resolution Coronal Imager Flight of 2018 May 29. *ApJ* **2020**, *896*, 51. https://doi.org/10.3847/1538-4357/ab917c.
49. Upendran, V.; Tripathi, D. On the Impulsive Heating of Quiet Solar Corona. *ApJ* **2021**, *916*, 59, [arXiv:astro-ph.SR/2103.16824]. https://doi.org/10.3847/1538-4357/abf65a.
50. Cargill, P.J. Some Implications of the Nanoflare Concept. *ApJ* **1994**, *422*, 381. https://doi.org/10.1086/173733.
51. Reale, F.; McTiernan, J.M.; Testa, P. Comparison of Hinode/XRT and RHESSI Detection of Hot Plasma in the Non-Flaring Solar Corona. *ApJL* **2009**, *704*, L58–L61, [arXiv:astro-ph.SR/0909.2529]. https://doi.org/10.1088/0004-637X/704/1/L58.
52. Schmelz, J.T.; Kashyap, V.L.; Saar, S.H.; Dennis, B.R.; Grigis, P.C.; Lin, L.; De Luca, E.E.; Holman, G.D.; Golub, L.; Weber, M.A. Some Like It Hot: Coronal Heating Observations from Hinode X-ray Telescope and RHESSI. *ApJ* **2009**, *704*, 863–869. https://doi.org/10.1088/0004-637X/704/1/863.
53. Winebarger, A.R.; Warren, H.P.; Schmelz, J.T.; Cirtain, J.; Mulu-Moore, F.; Golub, L.; Kobayashi, K. Defining the "Blind Spot" of Hinode EIS and XRT Temperature Measurements. *ApJL* **2012**, *746*, L17. https://doi.org/10.1088/2041-8205/746/2/L17.
54. Parenti, S.; del Zanna, G.; Petralia, A.; Reale, F.; Teriaca, L.; Testa, P.; Mason, H.E. Spectroscopy of Very Hot Plasma in Non-flaring Parts of a Solar Limb Active Region: Spatial and Temporal Properties. *ApJ* **2017**, *846*, 25, [arXiv:astro-ph.SR/1707.08445]. https://doi.org/10.3847/1538-4357/aa835f.
55. Del Zanna, G.; Andretta, V.; Cargill, P.J.; Corso, A.J.; Daw, A.N.; Golub, L.; Klimchuk, J.A.; Mason, H.E. High resolution soft X-ray spectroscopy and the quest for the hot (5-10 MK) plasma in solar active regions. *Frontiers in Astronomy and Space Sciences* **2021**, *8*, 33, [arXiv:astro-ph.SR/2103.06156]. https://doi.org/10.3389/fspas.2021.638489.
56. Bradshaw, S.J.; Del Zanna, G.; Mason, H.E. On the consequences of a non-equilibrium ionisation balance for compact flare emission and dynamics. *A&A* **2004**, *425*, 287–299. https://doi.org/10.1051/0004-6361:20040521.
57. Bradshaw, S.J.; Klimchuk, J.A. What Dominates the Coronal Emission Spectrum During the Cycle of Impulsive Heating and Cooling? *ApJS* **2011**, *194*, 26. https://doi.org/10.1088/0067-0049/194/2/26.

58. Dzifčáková, E.; Dudík, J.; Mackovjak, Š. Non-equilibrium ionization by a periodic electron beam. I. Synthetic coronal spectra and implications for interpretation of observations. *A&A* **2016**, *589*, A68, [arXiv:astro-ph.SR/1603.04256]. https://doi.org/10.1051/0004-6361/201527557.
59. Dudík, J.; Dzifčáková, E.; Meyer-Vernet, N.; Del Zanna, G.; Young, P.R.; Giunta, A.; Sylwester, B.; Sylwester, J.; Oka, M.; Mason, H.E.; et al. Nonequilibrium Processes in the Solar Corona, Transition Region, Flares, and Solar Wind (Invited Review). *Sol Phys* **2017**, *292*, 100, [arXiv:astro-ph.SR/1706.03396]. https://doi.org/10.1007/s11207-017-1125-0.
60. Lörinčík, J.; Dudík, J.; del Zanna, G.; Dzifčáková, E.; Mason, H.E. Plasma Diagnostics from Active Region and Quiet-Sun Spectra Observed by Hinode/EIS: Quantifying the Departures from a Maxwellian Distribution. *ApJ* **2020**, *893*, 34, [arXiv:astro-ph.SR/2003.07091]. https://doi.org/10.3847/1538-4357/ab8010.
61. Del Zanna, G.; Polito, V.; Dudík, J.; Testa, P.; Mason, H.E.; Dzifčáková, E. Diagnostics of Non-Maxwellian Electron Distributions in Solar Active Regions from Fe XII Lines Observed by the Hinode Extreme Ultraviolet Imaging Spectrometer and Interface Region Imaging Spectrograph. *ApJ* **2022**, *930*, 61. https://doi.org/10.3847/1538-4357/ac6174.
62. Jeffrey, N.L.S.; Fletcher, L.; Labrosse, N. First evidence of non-Gaussian solar flare EUV spectral line profiles and accelerated non-thermal ion motion. *A&A* **2016**, *590*, A99, [arXiv:astro-ph.SR/1601.07308]. https://doi.org/10.1051/0004-6361/201527986.
63. Jeffrey, N.L.S.; Fletcher, L.; Labrosse, N. Non-Gaussian Velocity Distributions in Solar Flares from Extreme Ultraviolet Lines: A Possible Diagnostic of Ion Acceleration. *ApJ* **2017**, *836*, 35, [arXiv:astro-ph.SR/1701.02196]. https://doi.org/10.3847/1538-4357/836/1/35.
64. Dudík, J.; Polito, V.; Dzifčáková, E.; Del Zanna, G.; Testa, P. Non-Maxwellian Analysis of the Transition-region Line Profiles Observed by the Interface Region Imaging Spectrograph. *ApJ* **2017**, *842*, 19, [arXiv:astro-ph.SR/1705.02104]. https://doi.org/10.3847/1538-4357/aa71a8.
65. Polito, V.; Dudík, J.; Kašparová, J.; Dzifčáková, E.; Reeves, K.K.; Testa, P.; Chen, B. Broad Non-Gaussian Fe XXIV Line Profiles in the Impulsive Phase of the 2017 September 10 X8.3-class Flare Observed by Hinode/EIS. *ApJ* **2018**, *864*, 63, [arXiv:astro-ph.SR/1807.09361]. https://doi.org/10.3847/1538-4357/aad62d.
66. Del Zanna, G. The multi-thermal emission in solar active regions. *A&A* **2013**, *558*, A73. https://doi.org/10.1051/0004-6361/201321653.
67. Li, W.; Li, M.; Wang, K.; Brage, T.; Hutton, R.; Landi, E. A Theoretical Investigation of the Magnetic-field-induced Transition in Fe X, of Importance for Measuring Magnetic Field Strengths in the Solar Corona. *ApJ* **2021**, *913*, 135. https://doi.org/10.3847/1538-4357/abfa97.
68. Chen, Y.; Li, W.; Tian, H.; Bai, X.; Hutton, R.; Brage, T. Application of a Magnetic-field-induced Transition in Fe X to Solar and Stellar Coronal Magnetic Field Measurements. *Research in Astronomy and Astrophysics* **2023**, *23*, 022001, [arXiv:astro-ph.SR/2212.02873]. https://doi.org/10.1088/1674-4527/acaa8e.
69. Del Zanna, G.; Mason, H.E. Solar UV and X-ray spectral diagnostics. *Living Reviews in Solar Physics* **2018**, *15*, 5, [arXiv:astro-ph.SR/1809.01618]. https://doi.org/10.1007/s41116-018-0015-3.
70. Landi, E.; Li, W.; Brage, T.; Hutton, R. Hinode/EIS Coronal Magnetic Field Measurements at the Onset of a C2 Flare. *ApJ* **2021**, *913*, 1, [arXiv:astro-ph.SR/2102.06072]. https://doi.org/10.3847/1538-4357/abf6d1.
71. Brooks, D.H.; Warren, H.P.; Landi, E. Measurements of Coronal Magnetic Field Strengths in Solar Active Region Loops. *ApJL* **2021**, *915*, L24, [arXiv:astro-ph.SR/2106.10884]. https://doi.org/10.3847/2041-8213/ac0c84.
72. Dudík, J.; Mackovjak, Š.; Dzifčáková, E.; Del Zanna, G.; Williams, D.R.; Karlický, M.; Mason, H.E.; Lörinčík, J.; Kotrč, P.; Fárník, F.; et al. Imaging and Spectroscopic Observations of a Transient Coronal Loop: Evidence for the Non-Maxwellian K Distributions. *ApJ* **2015**, *807*, 123, [arXiv:astro-ph.SR/1505.04333]. https://doi.org/10.1088/0004-637X/807/2/123.
73. Antonucci, E. Solar flare spectral diagnosis: Present and future. *Sol Phys* **1989**, *121*, 31–60. https://doi.org/10.1007/BF00161686.
74. Del Zanna, G.; Berlicki, A.; Schmieder, B.; Mason, H.E. A Multi-Wavelength Study of the Compact M1 Flare on October 22, 2002. *Sol Phys* **2006**, *234*, 95–113. https://doi.org/10.1007/s11207-006-0016-6.
75. Polito, V.; Testa, P.; De Pontieu, B. Can the Superposition of Evaporative Flows Explain Broad Fe XXI Profiles during Solar Flares? *ApJL* **2019**, *879*, L17. https://doi.org/10.3847/2041-8213/ab290b.

76. Bian, N.H.; Emslie, A.G.; Stackhouse, D.J.; Kontar, E.P. The Formation of Kappa-distribution Accelerated Electron Populations in Solar Flares. *ApJ* **2014**, *796*, 142, [arXiv:astro-ph.SR/1410.0819]. https://doi.org/10.1088/0004-637X/796/2/142.
77. Del Zanna, G.; Andretta, V.; Cargill, P.J.; Corso, A.J.; Daw, A.N.; Golub, L.; Klimchuk, J.A.; Mason, H.E. High resolution soft X-ray spectroscopy and the quest for the hot (5-10 MK) plasma in solar active regions. *Frontiers in Astronomy and Space Sciences* **2021**, *8*, 33, [arXiv:astro-ph.SR/2103.06156]. https://doi.org/10.3389/fspas.2021.638489.
78. Del Zanna, G.; Woods, T.N. Spectral diagnostics with the SDO EVE flare lines. *A&A* **2013**, *555*, A59. https://doi.org/10.1051/0004-6361/201220988.
79. Del Zanna, G.; Dere, K.P.; Young, P.R.; Landi, E. CHIANTI—An Atomic Database for Emission Lines. XVI. Version 10, Further Extensions. *ApJ* **2021**, *909*, 38, [arXiv:physics.atom-ph/2011.05211]. https://doi.org/10.3847/1538-4357/abd8ce.
80. Mondal, B.; Sarkar, A.; Vadawale, S.V.; Mithun, N.P.S.; Janardhan, P.; Del Zanna, G.; Mason, H.E.; Mitra-Kraev, U.; Narendranath, S. Evolution of Elemental Abundances during B-Class Solar Flares: Soft X-Ray Spectral Measurements with Chandrayaan-2 XSM. *ApJ* **2021**, *920*, 4, [arXiv:astro-ph.SR/2107.07825]. https://doi.org/10.3847/1538-4357/ac14c1.
81. Laming, J.M. The FIP and Inverse FIP Effects in Solar and Stellar Coronae. *Living Reviews in Solar Physics* **2015**, *12*, 2. https://doi.org/10.1007/lrsp-2015-2.
82. Doschek, G.A.; Feldman, U.; Kreplin, R.W.; Cohen, L. High-resolution X-ray spectra of solar flares. III - General spectral properties of X1-X5 type flares. *ApJ* **1980**, *239*, 725–737. https://doi.org/10.1086/158158.
83. Doschek, G.A.; Tanaka, K. Transient Ionization and Solar Flare X-Ray Spectra. *ApJ* **1987**, *323*, 799. https://doi.org/10.1086/165873.
84. Smith, R.K.; Hughes, J.P. Ionization Equilibrium Timescales in Collisional Plasmas. *ApJ* **2010**, *718*, 583–585, [arXiv:astro-ph.HE/1006.0254]. https://doi.org/10.1088/0004-637X/718/1/583.
85. Lee, J.Y.; Raymond, J.C.; Reeves, K.K.; Shen, C.; Moon, Y.J.; Kim, Y.H. Nonequilibrium Ionization Effects on Solar EUV and X-Ray Imaging Observations. *ApJ* **2019**, *879*, 111, [arXiv:astro-ph.SR/1905.11632]. https://doi.org/10.3847/1538-4357/ab24bb.
86. Olluri, K.; Gudiksen, B.V.; Hansteen, V.H. Non-equilibrium Ionization Effects on the Density Line Ratio Diagnostics of O IV. *ApJ* **2013**, *767*, 43. https://doi.org/10.1088/0004-637X/767/1/43.
87. Del Zanna, G. The multi-thermal emission in solar active regions. *A&A* **2013**, *558*, A73. https://doi.org/10.1051/0004-6361/201321653.
88. Calcines, A.; Wells, M.; O'Brien, K.; Morris, S.; Seifert, W.; Zanutta, A.; Evans, C.; Di Marcantonio, P. Design of the VLT-CUBES image slicers:. *Experimental Astronomy* **2023**, *55*, 267–280. https://doi.org/10.1007/s10686-022-09866-5.
89. Richard, J.; Bacon, R.; Jeanneau, A. BlueMUSE: science cases and requirements. In Proceedings of the Ground-based and Airborne Instrumentation for Astronomy VIII; Evans, C.J.; Bryant, J.J.; Motohara, K., Eds. International Society for Optics and Photonics, SPIE, 2020, Vol. 11447, p. 114470S. https://doi.org/10.1117/12.2561440.
90. Laurent, F.; Adjali, L.; Arns, J.; Bacon, R.; Boudon, D.; Caillier, P.; Daguisé, E.; Delabre, B.; Dubois, J.P.; Godefroy, P.; et al. MUSE integral field unit: test results on the first out of 24. In Proceedings of the Modern Technologies in Space- and Ground-based Telescopes and Instrumentation; Atad-Ettedgui, E.; Lemke, D., Eds., 2010, Vol. 7739, *Society of Photo-Optical Instrumentation Engineers (SPIE) Conference Series*, p. 77394M. https://doi.org/10.1117/12.857004.
91. Cuevas, S.; Eikenberry, S.S.; Sánchez, B. FRIDA integral field unit manufacturing. In Proceedings of the Advances in Optical and Mechanical Technologies for Telescopes and Instrumentation; Navarro, R.; Cunningham, C.R.; Barto, A.A., Eds. International Society for Optics and Photonics, SPIE, 2014, Vol. 9151, p. 91514N. https://doi.org/10.1117/12.2057442.
92. Calcines Rosario, A.; Dubbeldam, C.M.; Sharples, R.; Bourgenot, C.; Diaz, R.; Stephens, A.W. The HR image slicer for GNIRS at Gemini North: optical design and performance. In Proceedings of the Ground-based and Airborne Instrumentation for Astronomy IX; Evans, C.J.; Bryant, J.J.; Motohara, K., Eds., 2022, Vol. 12184, *Society of Photo-Optical Instrumentation Engineers (SPIE) Conference Series*, p. 121840L. https://doi.org/10.1117/12.2626235.

93. Laurent, F.; Boudon, D.; Kosmalski, J.; Loupias, M.; Raffault, G.; Remillieux, A.; Thatte, N.; Bryson, I.; Schnetler, H.; Clarke, F.; et al. ELT HARMONI: image slicer preliminary design. In Proceedings of the Ground-based and Airborne Instrumentation for Astronomy VII; Evans, C.J.; Simard, L.; Takami, H., Eds., 2018, Vol. 10702, *Society of Photo-Optical Instrumentation Engineers (SPIE) Conference Series*, p. 1070296, [arXiv:astro-ph.IM/1807.06313]. https://doi.org/10.1117/12.2312497.
94. Brandl, B.R.; Bettonvil, F.; van Boekel, R.; Glauser, A.; Quanz, S.P.; Absil, O.; Feldt, M.; Garcia, P.J.V.; Glasse, A.; Guedel, M.; et al. Status update on the development of METIS, the mid-infrared ELT imager and spectrograph. In Proceedings of the Ground-based and Airborne Instrumentation for Astronomy IX; Evans, C.J.; Bryant, J.J.; Motohara, K., Eds., 2022, Vol. 12184, *Society of Photo-Optical Instrumentation Engineers (SPIE) Conference Series*, p. 1218421. https://doi.org/10.1117/12.2628331.
95. Calcines, A.; López, R.L.; Collados, M. MuSICa: the Multi-Slit Image Slicer for the est Spectrograph. *Journal of Astronomical Instrumentation* **2013**, *2*, 1350009. https://doi.org/10.1142/S2251171713500098.
96. Calcines, A.; López, R.L.; Collados, M. a High Resolution Integral Field Spectrograph for the European Solar Telescope. *Journal of Astronomical Instrumentation* **2013**, *2*, 1350007. https://doi.org/10.1142/S2251171713500074.
97. Calcines, A.; López, R.L.; Collados, M.; Vega Reyes, N. MuSICa image slicer prototype at 1.5-m GREGOR solar telescope. In Proceedings of the Ground-based and Airborne Instrumentation for Astronomy V; Ramsay, S.K.; McLean, I.S.; Takami, H., Eds., 2014, Vol. 9147, *Society of Photo-Optical Instrumentation Engineers (SPIE) Conference Series*, p. 91473I. https://doi.org/10.1117/12.2053577.
98. Dubbeldam, C.M.; Robertson, D.J.; Ryder, D.A.; Sharples, R.M. Prototyping of diamond machined optics for the KMOS and JWST NIRSpec integral field units. In Proceedings of the Society of Photo-Optical Instrumentation Engineers (SPIE) Conference Series; Atad-Ettedgui, E.; Antebi, J.; Lemke, D., Eds., 2006, Vol. 6273, *Society of Photo-Optical Instrumentation Engineers (SPIE) Conference Series*, p. 62733F. https://doi.org/10.1117/12.669355.
99. Lee, D.; Wells, M.; Dickson, C.J.; Shore, P.; Morantz, P. Development of diamond machined mirror arrays for integral field spectroscopy. In Proceedings of the Society of Photo-Optical Instrumentation Engineers (SPIE) Conference Series; Atad-Ettedgui, E.; Antebi, J.; Lemke, D., Eds., 2006, Vol. 6273, *Society of Photo-Optical Instrumentation Engineers (SPIE) Conference Series*, p. 62731Y. https://doi.org/10.1117/12.673591.
100. Witt, E.M.; Fleming, B.T.; Green, J.C.; France, K.; Williams, J.; Sukegawa, T.; Siegmund, O.; Chafetz, D.; Tecza, M.; Levy, A.; et al. INFUSE: assembly and alignment of a rocket-borne FUV integral field spectrograph. In Proceedings of the UV, X-Ray, and Gamma-Ray Space Instrumentation for Astronomy XXII; Siegmund, O.H., Ed., 2021, Vol. 11821, *Society of Photo-Optical Instrumentation Engineers (SPIE) Conference Series*, p. 118210F. https://doi.org/10.1117/12.2594290.
101. Calcines-Rosario, A.; Matthews, S.; Reid, H. Exploring the application of image slicers for the EUV for the next generation of solar space missions. In Proceedings of the Space Telescopes and Instrumentation 2022: Ultraviolet to Gamma Ray; den Herder, J.W.A.; Nikzad, S.; Nakazawa, K., Eds., 2022, Vol. 12181, *Society of Photo-Optical Instrumentation Engineers (SPIE) Conference Series*, p. 121810K. https://doi.org/10.1117/12.2626860.
102. De Pontieu, B.; Martínez-Sykora, J.; Testa, P.; Winebarger, A.R.; Daw, A.; Hansteen, V.; Cheung, M.C.M.; Antolin, P. The Multi-slit Approach to Coronal Spectroscopy with the Multi-slit Solar Explorer (MUSE). *ApJ* **2020**, *888*, 3, [arXiv:astro-ph.IM/1909.08818]. https://doi.org/10.3847/1538-4357/ab5b03.
103. De Pontieu, B.; Testa, P.; Martínez-Sykora, J.; Antolin, P.; Karampelas, K.; Hansteen, V.; Rempel, M.; Cheung, M.C.M.; Reale, F.; Danilovic, S.; et al. Probing the Physics of the Solar Atmosphere with the Multi-slit Solar Explorer (MUSE). I. Coronal Heating. *ApJ* **2022**, *926*, 52, [arXiv:astro-ph.SR/2106.15584]. https://doi.org/10.3847/1538-4357/ac4222.
104. Cheung, M.C.M.; Martínez-Sykora, J.; Testa, P.; De Pontieu, B.; Chintzoglou, G.; Rempel, M.; Polito, V.; Kerr, G.S.; Reeves, K.K.; Fletcher, L.; et al. Probing the Physics of the Solar Atmosphere with the Multi-slit Solar Explorer (MUSE). II. Flares and Eruptions. *ApJ* **2022**, *926*, 53, [arXiv:astro-ph.SR/2106.15591]. https://doi.org/10.3847/1538-4357/ac4223.
105. Calcines, A.; Bourgenot, C.; Sharples, R. Design of freeform diffraction gratings: performance, limitations and potential applications. In Proceedings of the Advances in Optical and Mechanical Technologies for Telescopes and Instrumentation III; Navarro, R.; Geyl, R., Eds. International Society for Optics and Photonics, SPIE, 2018, Vol. 10706, p. 107064Z. https://doi.org/10.1117/12.2312125.

106. Bourgenot, C.; Robertson, D.J.; Stelter, D.; Eikenberry, S. Towards freeform curved blazed gratings using diamond machining. In Proceedings of the Advances in Optical and Mechanical Technologies for Telescopes and Instrumentation II; Navarro, R.; Burge, J.H., Eds., 2016, Vol. 9912, *Society of Photo-Optical Instrumentation Engineers (SPIE) Conference Series*, p. 99123M. https://doi.org/10.1117/12.2231182.
107. Shimizu, T.; Imada, S.; Kawate, T.; Ichimoto, K.; Suematsu, Y.; Hara, H.; Katsukawa, Y.; Kubo, M.; Toriumi, S.; Watanabe, T.; et al. The Solar-C_EUVST mission. In Proceedings of the UV, X-Ray, and Gamma-Ray Space Instrumentation for Astronomy XXI; Siegmund, O.H., Ed., 2019, Vol. 11118, *Society of Photo-Optical Instrumentation Engineers (SPIE) Conference Series*, p. 1111807. https://doi.org/10.1117/12.2528240.
108. Corso, A.J.; Pelizzo, M.G. Extreme ultraviolet multilayer nanostructures and their application to solar plasma observations: A review. *Journal of nanoscience and nanotechnology* **2019**, *19*, 532–545. https://doi.org/10.1166/jnn.2019.16477.
109. Corso, A.J.; Del Zanna, G.; Polito, V. Future perspectives in solar hot plasma observations in the soft X-rays. *Experimental Astronomy* **2021**, *51*, 453–474. https://doi.org/10.1007/s10686-021-09756-2.